JGR Oceans

RESEARCH ARTICLE
10.1029/2020JC016947

Multi-Year Estimates of Daily Heat Transport by the Atlantic Meridional Overturning Circulation at 34.5°S

M. Kersalé[1,2], C. S. Meinen[2], R. C. Perez[2], A. R. Piola[3,4,5], S. Speich[6], E. J. D. Campos[7,8], S. L. Garzoli[2], I. Ansorge[9], D. L. Volkov[1,2], M. Le Hénaff[1,2], S. Dong[2], T. Lamont[9,10,11], O. T. Sato[7], and M. van den Berg[10]

[1]Cooperative Institute for Marine and Atmospheric Studies, University of Miami, Miami, FL, USA, [2]NOAA Atlantic Oceanographic and Meteorological Laboratory, Miami, FL, USA, [3]Servicio de Hidrografía Naval, Buenos Aires, Argentina, [4]Instituto Franco-Argentino sobre Estudio del Clima y sus Impactos (UMI-IFAECI/CNRS-CONICET-UBA), Buenos Aires, Argentina, [5]Universidad de Buenos Aires, Buenos Aires, Argentina, [6]Laboratoire de Météorologie Dynamique–IPSL, Ecole Normale Supérieure, Paris, France, [7]Oceanographic Institute, University of São Paulo, São Paulo, Brazil, [8]Department of Biology, Chemistry and Environmental Sciences, School of Arts and Sciences, American University of Sharjah, Sharjah, United Arab Emirates, [9]Department of Oceanography, University of Cape Town, Rondebosch, South Africa, [10]Department of Environment, Forestry and Fisheries, Oceans and Coasts Research Branch, Cape Town, South Africa, [11]Bayworld Centre for Research and Education, Cape Town, South Africa

Key Points:

- Implementation of a novel methodology for computing the daily meridional heat transport time series at 34.5°S from 2013 to 2017
- The heat transport has significant variability highly correlated with changes in the strength of the meridional overturning circulation
- A reconstructed/extended meridional heat transport time series allows analysis of seasonal to interannual changes and long-term trend

Correspondence to:
M. Kersalé,
marion.kersale@gmail.com

Citation:
Kersalé, M., Meinen, C. S., Perez, R. C., Piola, A. R., Speich, S., Campos, E. J. D., et al. (2021). Multi-year estimates of daily heat transport by the Atlantic meridional overturning circulation at 34.5°S. *Journal of Geophysical Research: Oceans*, *126*, e2020JC016947. https://doi.org/10.1029/2020JC016947

Received 30 OCT 2020
Accepted 30 MAR 2021

Abstract Variations in the mass and heat transported by the meridional overturning circulation (MOC) have important, well-documented, influences on global and regional climate, weather, ecosystems, and coastal sea levels. However, continuous, high-frequency, observations of these quantities have been limited to date. Multiple years of full-depth daily observations from moored instruments in the South Atlantic at 34.5°S are combined with satellite observations to resolve the volume transports in both the upper and abyssal MOC cells, and the associated full-depth meridional heat transport (MHT), on daily to interannual timescales. A newly developed method for combining satellite sea level observations with historical hydrographic measurements was used to estimate daily full-depth ocean profiles of temperature in the ocean interior where mooring coverage is sparse. The average MHT during 2013–2017 is 0.5 PW, with a daily standard deviation of 0.8 PW. The MHT variability is most strongly driven by the geostrophic relative velocity contributions (horizontal density-gradient changes). This variability is highly correlated with the volume transport variability of the MOC upper cell ($r = 0.96$) and modestly anti-correlated ($r = -0.52$) with the abyssal cell variations. An empirical relationship between the MHT and MOC values was developed allowing the reconstruction of a longer MHT time series including the pilot array period (2009–2010). Seasonal variation of the MHT is significant, and results from strong variations of all terms (Ekman, barotropic, and baroclinic). Although the 2013–2017 shows an increasing MHT trend (0.14 PW/year), the longer time period record suggests that the apparent trend may simply be interannual modulation of MHT at 34.5°S.

Plain Language Summary Changes in the meridional overturning circulation, a large system of ocean currents driven by differences in temperature and salt content as well as the winds, are known to have significant influences on the global climate system. This study presents, for the first time, full-depth, daily measurements of the volume and heat transported by this circulation system in the South Atlantic at 34.5°S based on direct observations. As the instruments anchored on the seafloor are too widely spaced in the basin interior, a new method for using satellite observations to estimate interior temperature profiles was developed and used. The roughly 4 years of continuous daily data reveal seasonal and interannual changes of these important flows. The observations also demonstrate that the volume and heat transports vary in a consistent manner with one another. This allows us to use some earlier moored observations from a pilot version of the array, extending the data record further back in time and producing ~6 years of daily estimates of heat transport in the South Atlantic during 2009–2017, with a gap during 2010–2013.

1. Introduction

The oceans absorb more than 90% of the excess heat gained by the Earth's climate system (Johnson & Lyman, 2020; Levitus et al., 2012; Rhein et al., 2013). Ocean currents redistribute the excess heat from

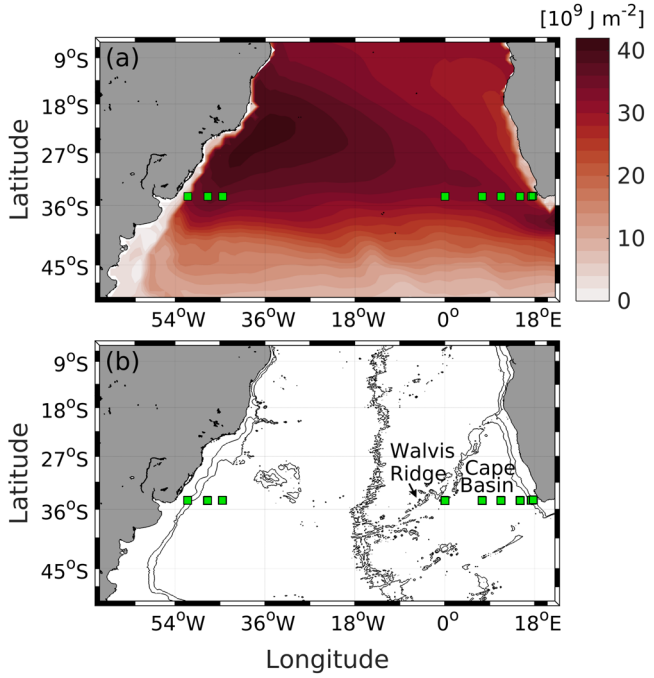

Figure 1. Array locations and heat content in the South Atlantic. (a) South Atlantic MOC Basin-wide Array (SAMBA) mooring locations used in this study (green squares) superimposed onto the mean ocean heat content from 0 to 700 m depth from September 2013 to July 2017 (heat content data provided by Cheng et al. [2017] shaded colors). (b) Topographic features are identified with black contours characterizing the 1,000 and 3,000 m isobaths.

low latitudes polewards primarily via the meridional overturning circulation (MOC) (e.g., Talley, 2003). The MOC pathways in the North Atlantic Ocean are responsible for more than half of the total poleward heat transport carried in the global ocean (Johns et al., 2011; Lavin et al., 1998; Talley, 2003), despite the fact that the Atlantic is so much narrower than the Pacific and Indian basins together. Within the South Atlantic Ocean, the northward MOC flows supplied by the heat advected from the Indian Ocean are strong enough to reverse the expected poleward heat transport observed in all other major ocean basins, yielding a unique equatorward net heat transport (e.g., Ganachaud & Wunsch, 2000; Garzoli & Baringer, 2007; Talley, 2003). Ocean and climate models suggest that variations in the MOC volume transport, and in the associated meridional heat transport (MHT), in the South Atlantic modulate inter-hemispheric global atmospheric circulations on decadal timescales, with profound impacts on regional and global climate (e.g., Lopez et al., 2016). The rate at which heat is transported northward compared to being stored by the South Atlantic subtropical gyre is also of great importance (e.g., Willis et al., 2004; Wu et al., 2012), and changes in the South Atlantic ocean are thought to play a significant role in the establishment of oceanic teleconnections (e.g., Xue, Li, et al., 2018; Xue, Sun, et al., 2018).

Within the South Atlantic Ocean, the upper MOC cell is characterized by a northward transport of relatively warm waters within roughly the upper 1,300 m that is compensated by a southward upper branch of relatively cold North Atlantic Deep Water (NADW) between ~1,300 and 3,150 m (e.g., Kersalé, Meinen, et al., 2020; Lumpkin & Speer, 2007; Talley, 2003). The warm upper limb of the upper MOC cell is a complex blend of waters originating from the Indian and Pacific Oceans that flows into the Atlantic basin around the southern tip of Africa and via Drake Passage, respectively, and which then transits to the north primarily through the Cape Basin (e.g., Bower et al., 2019; de Ruijter et al., 1999; Rousselet et al., 2020; Rühs et al., 2019; Sloyan & Rintoul, 2001). The cold lower limb of the upper MOC cell flows southward through the South Atlantic basin along the western and eastern boundaries (e.g., Bower et al., 2019; Garzoli, Dong, et al., 2015; Kersalé, Perez, et al., 2019; Meinen, Garzoli, et al., 2017). Below this upper MOC cell is a deeper, abyssal MOC cell that is characterized by a northward flow of very cold Antarctic bottom water (AABW) below about 4,300 m that is compensated by a southward lower branch of cold NADW (but comparatively warmer compared to AABW) between roughly 3,150 and 4,300 m (e.g., Cessi, 2019; Kersalé, Meinen, et al., 2020). The northward flowing deep limb of the abyssal MOC cell is concentrated in the western portion of the basin due to the topographic barrier of the Walvis Ridge (shown in Figure 1) (e.g., Coles et al., 1996; Valla et al., 2019), while the southward return flow in the abyssal MOC cell merges with the southward flowing lower limb of the upper MOC cell (e.g., Ganachaud & Wunsch, 2000; Kersalé, Meinen, et al., 2020). This complicated vertical-horizontal flow structure in the South Atlantic has implications for the calculation of MHT. Note, the MOC flow pattern is less complicated in the subtropical North Atlantic, where the abyssal MOC cell is extremely weak (e.g., Frajka-Williams, Cunningham, et al., 2011) and can in essence be neglected in calculating the MHT (e.g., Johns et al., 2011).

The majority of historical estimates of the volume transport of the MOC have focused only on the flow in the upper cell of the MOC, while the flow in the abyssal cell of the MOC has often been neglected. Hereafter in this document the notation "MOC_{up}" will be used when specifically discussing the upper MOC cell, and "MOC_{ab}" will be used when specifically discussing the abyssal MOC cell; "MOC" will be used without a subscript notation when discussing the complete (i.e., full-depth) overturning system. In addition to neglecting MOC_{ab}, most previous estimates of the MOC and MHT in the South Atlantic have been derived from infrequent trans-basin observations from ships, including quasi-decadal full-depth conductivity-temperature-depth (CTD) sections (e.g., Bryden et al., 2011; Hernández-Guerra et al., 2019; McDonagh & King, 2005; Saunders & King, 1995), eXpendable BathyThermograph (XBT) transects carried

out roughly four times per year since 2002 (e.g., Dong, Garzoli, Baringer, Meinen, & Goni, 2009; Garzoli & Baringer, 2007; Garzoli, Baringer, et al., 2013), or inverse models combining multiple hydrographic sections (de las Heras & Schlitzer, 1999; Ganachaud & Wunsch, 2003; Lumpkin & Speer, 2007). Monthly estimates since 1993 have also been made using blended satellite altimetry and irregularly distributed in space and time Argo float data (Dong, Goni, & Bringas, 2015; Majumder et al., 2016). These available historical estimates of the MOC (which are really only estimates of the MOC_{up}) and MHT between 30°S and 45°S show a wide range of values, about 18.1–23.4 Sv and −0.23 to 0.76 PW, respectively (de las Heras & Schlitzer, 1999; Garzoli, Baringer, et al., 2013; Majumder et al., 2016). The corresponding estimates of the variability are also quite diverse with standard deviations ranging from 2.3 to 4.6 Sv and 0.08 to 0.22 PW, respectively (Garzoli, Baringer, et al., 2013; Majumder et al., 2016; McDonagh & King, 2005). While these historical records have unquestionably expanded our understanding of the oceanic fluxes across multiple latitudes in the region, continuous multi-year daily records of the MOC and MHT in the upper-ocean of the North Atlantic have shown that these transports are highly variable with considerable energy at sub-monthly frequencies (e.g., Johns et al., 2011; Kanzow, Cunningham, Johns, et al., 2010). As such, it is evident that synoptic (snapshot) observations and/or monthly gridded products may miss important facets of MOC and MHT variability, inevitably leading to biased estimates.

To address this observational gap, moored arrays have been deployed at several latitudes as part of an international initiative to study the South Atlantic MOC (SAMOC; Ansorge et al., 2014; Garzoli & Matano, 2011; Herrford et al., 2021; Hummels et al., 2015; Kersalé, Meinen, et al., 2020; Kopte et al., 2017; Meinen, Speich, Perez, et al., 2013; Meinen, Speich, Piola, et al., 2018). One of the major components of this initiative is the South Atlantic MOC Basin-wide Array (SAMBA; Figure 1). SAMBA has been under construction since the initial pilot experiments in 2008–2009. The array consists primarily of Pressure-equipped Inverted Echo Sounder (PIES) moorings along 34.5°S, some of which are also equipped with a near-bottom current meter (CPIES), as well as four tall moorings close to the eastern boundary (e.g., Kersalé, Lamont, et al., 2018). Located at the entrance into the South Atlantic, the array captures most of the structure and variability of both the upper and the abyssal MOC cells (Kersalé, Meinen, et al., 2020). SAMBA was designed to capture the key basin-wide surface-to-seafloor ocean flows across 34.5°S, and the array is ideally situated to monitor exchanges of heat between the South Atlantic, Pacific, and Indian oceans, and to evaluate the associated MOC and MHT variability. Further analyses using numerical models have suggested that the observed warming trend of the Atlantic Ocean since the 1950s (Lee et al., 2011) and the MOC/MHT interannual to decadal variability (Dong, Garzoli, & Baringer, 2011) are largely due to inter-basin heat transport from the Indian Ocean. Thus, it is important to study volume and heat transport variability in this key region to understand warming in the Atlantic Ocean relative to the warming in the other ocean basins.

Analyses of the first few years of data from the pilot configuration of SAMBA have suggested that the MOC at 34.5°S is highly variable at time scales ranging from a few days to a year (Meinen, Speich, Perez, et al., 2013; Meinen, Speich, Piola, et al., 2018). Using a larger number of SAMBA moorings along this latitude rather than just the pilot moorings near the boundaries allows for better accuracy for the volume transport estimates as well as a better physical and statistical evaluation of the observed variations (Kersalé, Meinen, et al., 2020). While the moored instruments provide unprecedented temperature and salinity information near the western and eastern boundaries (e.g., Kersalé, Lamont, et al., 2018; Kersalé, Perez, et al., 2019; Meinen, Garzoli, et al., 2017; Valla et al., 2018, 2019), observations of temperature and salinity in the interior of the basin are still very sparse (Figure 1). This lack of moored observations in the basin interior is not a major challenge for MOC estimation as the volume transports are largely determined using geostrophic methods that integrate between moorings as is done for all of the major MOC arrays (e.g., Herrford et al., 2021; Kanzow, Cunningham, Rayner, et al., 2007; Meinen, Speich, Perez, et al., 2013; McCarthy, Smeed, et al., 2015). For the MHT calculation, however, a lack of information in the interior poses a serious shortcoming, as calculating the MHT requires estimates of zonally averaged temperatures profiles in the interior (e.g., Johns et al., 2011).

In the present study, we generate for the first time a daily MHT time series derived from SAMBA measurements and satellite observations for the period from September 2013 to July 2017. This MHT calculation involves the development and implementation of a novel synthesis of in situ and satellite altimetry data in order to estimate basin interior temperatures across 34.5°S in the South Atlantic to enhance the moored

observations near the basin boundaries. In addition, an analysis of the MOC variability from the SAMBA full array configuration period in 2013–2017 is presented, along with some comparisons to the pilot array configuration following Meinen, Speich, Piola, et al. (2018). An empirical relationship between the MHT and MOC values is developed that allows for the reconstruction of a longer MHT time series in 2009–2010 using the pilot array MOC time series. The fully resolved and reconstructed MHT data sets are compared with each other as well as to concurrent observations from independent observing systems.

2. Data and Methods

2.1. Atlantic MOC Volume Transport

2.1.1. Absolute Meridional Velocity From SAMBA

To assess the temporal variability of the MOC in the South Atlantic, we used a subset of the PIES/CPIES moorings along the SAMBA line at 34.5°S, for which data were continuously available from September 2013 to July 2017 (green squares in Figure 1). Since we do not need to use the near-bottom current meter data from the CPIES for the purposes of this study, hereafter we simply refer to the CPIES as PIES. The PIES moorings capture the ocean flows near the western and eastern boundaries along the continental slopes; the eastern array extends offshore to the Walvis Ridge. The depths of the PIES moorings range from 1,300 to 5,200 m, although only two moorings in the Cape Basin lie below 4,900 m. Hydrographic measurements are also collected along both the western and eastern PIES arrays during the mooring servicing cruises. These moored and hydrographic observations provide important insights into the local MOC flow patterns and water mass properties, and offer an updated view of the deep and abyssal flows along the boundaries (e.g., Kersalé, Lamont, et al., 2018; Kersalé, Meinen, et al., 2020; Kersalé, Perez, et al., 2019; Meinen, Speich, Perez, et al., 2013; Meinen, Speich, Piola, et al., 2018; Valla et al., 2018, 2019).

A PIES measures the bottom pressure, and the time for an acoustic signal to travel round-trip from the bottom-moored instrument to the sea surface and back (τ). In this study, PIES are used to estimate full water column profiles of temperature, salinity, and density at each mooring site via hydrography-derived lookup tables using the gravest empirical mode (GEM) method developed by Meinen and Watts (2000). Previously, these analyses have been successfully employed on the South Atlantic western boundary (e.g., Meinen, Garzoli, et al., 2017; Valla et al., 2019), eastern boundary (Kersalé, Lamont, et al., 2018; Kersalé, Perez, et al., 2019), as well as both boundaries jointly (Kersalé, Meinen, et al., 2020; Meinen, Speich, Perez, et al., 2013; Meinen, Speich, Piola, et al., 2018). Data from 378 CTD and 5,215 Argo profiles near the eastern boundary and from 485 CTD and 3,332 Argo profiles near the western boundary (all of the available profiles from January 1983 to December 2018) are used to create these lookup tables. The CTD/Argo data sets used for the GEM fields in the east span the region zonally bounded by 2°W and the South African continental shelf and meridionally bounded by 37°S and 31°S, while the data in the west span the region between the continental shelf to 40°W, and the same latitude range. The hydrographic data used to estimate temperature in the interior will be described in Section 2.2.1.

The density profiles derived via the GEM method can be vertically integrated to yield dynamic height anomaly profiles, and the component of the relative baroclinic velocity orthogonal to the line between each pair of PIES moorings can be calculated via geostrophy (i.e., the thermal wind relationship). The barotropic contribution can similarly be estimated as the geostrophic gradient between the measured bottom pressures at each instrument. The pressure differences yield absolute velocity fluctuations but not the time-mean (e.g., Donohue et al., 2010); the time-mean can be added from ancillary in situ observations (e.g., near-bottom current meters) or from a numerical model output. Combining the absolute reference velocity with the relative velocity produces full water column absolute velocity profiles of the component perpendicular to the mooring line. Because the present study does not use a residual method, and obtains the reference (barotropic) velocity variability directly from data (bottom pressure gradients), no "residual" zero net volume transport assumption is made here. In other words, the velocities are not uniformly adjusted to ensure zero net volume transport as in previous observational studies at other latitudes (e.g., Johns et al., 2011; McCarthy, Smeed, et al., 2015). As detailed in the following sections, estimates of the meridional Ekman flow (surface wind-driven) and the flow inshore of the shallowest moorings on either side of the basin are

added to the geostrophic component to yield the total absolute meridional velocity. The accuracies of the 34.5°S MOC estimates and its components are detailed in the Appendix.

2.1.2. Meridional Ekman Flow

Zonal wind stress data available from the cross-calibrated multi-platform (CCMP) wind product (e.g., Mears et al., 2019), which merges existing satellite scatterometer and microwave radiometer observations, are used to generate daily estimates of meridional Ekman transport across 34.5°S from September 2013 to July 2017 (e.g., Kersalé, Meinen, et al., 2020). Note, when we update the MOC estimate from the pilot configuration (Meinen, Speich, Perez, et al., 2013; Meinen, Speich, Piola, et al., 2018), we also use CCMP zonal wind stress from 2009 to 2010. Nevertheless, it has been shown that at 34.5°S different wind products generate similar values for the Ekman transport (Garzoli & Baringer, 2007), while at other latitudes (e.g., 11°S, Herrford et al., 2021) the choice of the wind product might be critical.

2.1.3. Time-Mean Reference Flow and Boundary Flows

As mentioned above, the bottom pressure gradients from the PIES only provide information about the temporal variations of the barotropic (reference) flow and cannot be used to estimate the time-mean due to the well-known leveling problem (e.g., Donohue et al., 2010). The time-mean reference geostrophic velocity between pairs of PIES was derived at 1,500 dbar from the time-mean of a 26-year run of the eddy-permitting Estimating the Circulation and Climate of the Ocean, Phase 2 (ECCO2; https://ecco.jpl.nasa.gov/) ocean state estimate (e.g., Menemenlis et al., 2005).

The ECCO2 output was also used to provide a time-invariant estimate of the volume fluxes on the continental shelves/upper slopes inshore of the shallowest moorings following previous methods (Kersalé, Meinen, et al., 2020). Note, similar results are reached when output from the Ocean general circulation model For the Earth Simulator (OFES; Masumoto et al., 2004; Sasaki et al., 2008) was used instead to provide the time-mean reference and boundary flows (Meinen, Speich, Perez, et al., 2013; Meinen, Speich, Piola, et al., 2018), demonstrating that the choice of model did not significantly influence our findings.

2.1.4. Pilot Array Versus Full Array Configuration

The resulting basin-wide meridional absolute velocity was then zonally and vertically integrated, and the transport of the basin-wide MOC strength and vertical structure was estimated (Figure 2a). The first MOC estimates using SAMBA mooring data only used two moorings (Sites A and Z, which are located near the ~1,300 m isobath, pilot array—red squares in Figure 2b) to estimate the strength of the MOC_{up} cell (e.g., Meinen, Speich, Perez, et al., 2013). The initial ~20-month long time series of the MOC_{up} volume transport from the pilot array between 2009 and 2010 was updated with an additional ~4 years of data at these two sites between 2013 and 2017 (Meinen, Speich, Piola, et al., 2018). Further analysis using all of the available moorings across 34.5°S (red and green symbols in Figure 2b) from September 2013 to July 2017 (the better-resolved PIES array began in 2013) has provided a more detailed understanding of the full-depth vertical, horizontal, and temporal structure of the MOC_{up}, as well as providing the ability to estimate MOC_{ab} (see next section). The methodology for estimating the full-depth MOC with the better-resolved mooring configuration was described in detail in Kersalé, Meinen, et al. (2020).

To illustrate the value of the enhanced, better-resolved, array configuration, we provide here a few statistics and comparisons of the time-mean MOC_{up} vertical structure at 34.5°S from these two configurations. The pilot array data from the original study of Meinen, Speich, Perez, et al. (2013) have been reanalyzed here using the same methodology as was applied by Kersalé, Meinen, et al. (2020) to the full array configuration (i.e., ECCO2 model output was used for the time-mean reference velocity flow and for the time-mean shelf flows inshore of the shallowest moorings). As is standard for nearly all estimates of the MOC_{up} cell (e.g., Frajka-Williams, Ansorge, et al., 2019; McCarthy, Brown, et al., 2020), the strength of the MOC_{up} flow is defined as the basin-wide transport integrated from the surface down to the time-mean pressure interface where the zonally integrated meridional flow changes from northward to southward (1,315 dbar here at 34.5°S for both configurations as in Kersalé, Meinen, et al. [2020]). The mean MOC_{up} strength determined here for the pilot array configuration over the period 2013–2017 is 17.7 Sv (red line in Figure 2a). Using the better resolution of nine moorings across 34.5°S, a somewhat weaker time-mean upper cell (17.3 Sv, green line in Figure 2a) is found, however, this mean difference is within the range of the error estimates for the

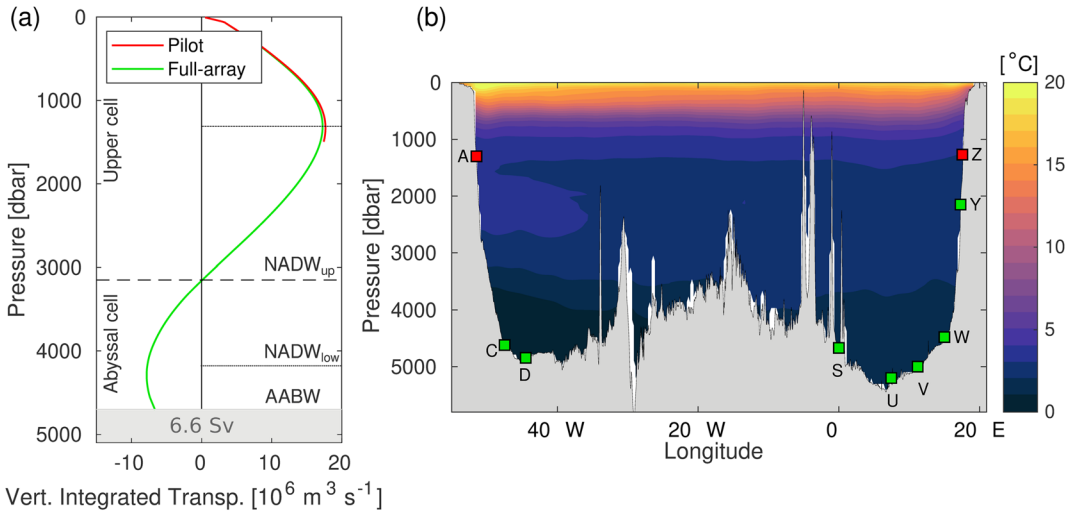

Figure 2. Time-mean volume transport and temperature section across SAMBA. (a) Time-mean cumulative transport as function of depth. The red line is the mean calculated using the SAMBA pilot deployment over the period September 2013 to July 2017, while the green line is the mean using the SAMBA full array configuration. The upper and abyssal Atlantic overturning cells are indicated on the left side of the panel with the upper and lower North Atlantic Deep Water and Antarctic bottom water branches on the right side. (b) Temperature section from the World Ocean Atlas (WOA) 2018 climatology with 0.25° horizontal resolution (Locarnini et al., 2019). Locations of the SAMBA moorings are represented as squares (red: Sites used in pilot configuration calculations; red and green: Sites used in full array configuration calculations).

calculations (Kersalé, Meinen, et al., 2020). These time-mean values are dependent on a numerical model (time-mean reference velocity flow at 1,500 dbar), but they are both reasonably close to previous mean MOC estimates determined from repeated XBT sections, which range from 17.9 to 18.1 Sv (Dong, Garzoli, Baringer, Meinen, & Goni, 2009; Garzoli, Baringer, et al., 2013).

2.1.5. Estimating the Abyssal Cell Transport

Another advantage of using the full 9-instrument resolution for the array is that, because the moorings span the entire water column, it allows determining not only the strength of the volume transport in the MOC_{up} cell, but also for the daily time-varying strength of the MOC_{ab} cell volume transport (Kersalé, Meinen, et al., 2020). The strength of the MOC_{ab} cell is defined as the volume transport integrated between 3,150 and 4,300 dbar (Kersalé, Meinen, et al., 2020), which represents the vertical layer just below the base of the MOC_{up} cell and above the depth where the meridional flow transitions from southward in the NADW layer to northward in the AABW layer, that is, measuring the upper limb of the MOC_{ab} cell. The time-mean of the maximum southward transport is roughly 7.8 Sv (Kersalé, Meinen, et al., 2020), falling within the 1.8–10.4 Sv range of previous estimates of the strength of the MOC_{ab} cell derived from snapshot ship sections at 30°S-32°S (Hernández-Guerra et al., 2019; Lumpkin & Speer, 2007).

The fully resolved array at 34.5°S allows transport calculations from the surface down to 4,700 dbar, which is the deepest common depth of the interior moorings (Sites D and S; see Figure 2b), yielding a time-mean southward transport of 6.6 ± 2.7 Sv integrated between the surface and this depth (Figure 2a). This mean flow should equal the northward flow that crosses 34.5°S between 4,700 dbar and the seafloor to close the mass budget which is consistent with the 30°S CTD section analysis that constrained the solution to have 7 ± 2 Sv of AABW flowing north in the western basin (Ganachaud & Wunsch, 2003), as well as prior estimates from inverse models that analyzed snapshot hydrographic sections (i.e., Lumpkin & Speer, 2007). Recall, however, that we directly estimate absolute geostrophic velocity fluctuations here and, hence no "residual" zero net volume transport assumption is made for volume transport. However, as it is understood that to compute meaningful estimates of heat transport there must be an underlying zero net mass balance (e.g., Baringer & Garzoli, 2007; Macdonald & Baringer, 2013), we must account for the unobserved contribution to the heat transport in the deep/abyssal ocean below 4,700 dbar (see Section 2.2.2 for details).

2.2. MHT Estimates

To determine daily estimates of the MHT across 34.5°S, the absolute meridional velocity derived from the full configuration of SAMBA as discussed in Section 2.1.1 must be combined with temperature data across the basin. We break the total heat transport down into a number of components:

$$Q_{\text{net}} = Q_{WB} + Q_{EB} + Q_{\text{midocean}} + Q_{\text{shelves}} + Q_{\text{deep}} \quad (1)$$

The different terms represent, respectively, the contribution to the total MHT (Q_{net}) by the flows near the western boundary between Sites A and D (Q_{WB}); the flows near the eastern boundary between Sites S and Z (Q_{EB}); the flows in the interior of the basin between Sites D and S (Q_{midocean}); the flows on the western and eastern shelves inshore of the shallowest moorings (Q_{shelves}); and the flow in the deep/abyssal ocean below 4,700 dbar (Q_{deep}). Note that the MHT is not separated into variations associated with the MOC_{up} cell and the MOC_{ab} cell—because the time-varying nature of the interfaces between the northward and southward flows at the various levels makes discriminating between those flows in a mass-conserving manner every day difficult. Instead, the MHT results presented here discuss the net heat transported by the full water column. The individual temperature transport terms in Equation 1 are defined by:

$$\int\int \rho C_p v\, \theta\, dxdz \quad (2)$$

with ρ the sea seawater density, C_p the specific heat of seawater, v the meridional velocity, and θ the potential temperature. A constant value of $\rho C_p = 4.1 \times 10^6$ J kg^{-1} °C^{-1} is used in all temperature transport calculations (similar to Johns et al., 2011).

This calculation is pretty straightforward for (Q_{WB}) and (Q_{EB}) using the geostrophic transports calculated between each pair of PIES and the simple zonal average of the temperature profiles at the pair of PIES mooring sites. The daily values of the zonally averaged temperature profiles are multiplied by the geostrophic velocity profiles and the result is then integrated between the surface and 4,700 dbar. The temperature transports are summed up according to the different geographical limits using Sites A, C, and D for (Q_{WB}) and Sites S, U, V, W, Y, and Z for (Q_{EB}). For (Q_{midocean}), PIES D and S are sufficient to monitor the basin-wide geostrophic transport, but the horizontal mooring resolution is too sparse to realistically represent the zonally averaged mid-ocean temperature profiles between Sites D and S. Methods to overcome this temperature data deficiency in the interior, as well as the estimation of the time-invariant temperature transports over the shelves and in the deep ocean below 4,700 dbar, are described in the following sections.

2.2.1. Mid-Ocean Temperature

To construct suitably accurate estimates of the zonally averaged temperature between Sites D and S at the highest possible temporal resolution concurrent with the corresponding daily geostrophic velocities, we will take advantage of the daily sea level anomaly (SLA) observations provided by gridding satellite altimetry across the interior of the basin. A gridded SLA product, provided by Copernicus Marine Environment Monitoring Service (CMEMS; http://marine.copernicus.eu/) for the same time period as the moored data, was used in this study. This gridded and interpolated product, generally known as the AVISO product, covers the global ocean with a horizontal and temporal resolution of 1/4° and 1 day, respectively, even if the original time scales represented are ~2–3 weeks due to spatiotemporal filtering (e.g., Ballarotta et al., 2019). As variations in steric sea level contribute significantly to sea level changes, SLA will be used as a direct proxy for dynamic height anomalies (DHA).

Available hydrographic data, between 38°W and 0°E and between 29°S and 37°S, are used to create an empirical two-dimensional lookup table relating temperature to pressure and DHA in the interior (Figure 3a). This is similar to the GEM method previously mentioned in Section 2.1 as developed by Meinen and Watts (2000), and to the GEM-ETTA (Enhanced Thermohaline Transport Analysis) technique developed by Byrne (2000) extending the GEM with a third dimension to include sea surface height. However, the new technique presented herein is distinct from those previous methods as it relates the temperature, for example, purely as a function of pressure and DHA. In the mid-ocean region, Argo is the main source of hydrographic data available for building the two-dimensional lookup tables (14,864 profiles), as full-depth CTD casts have only rarely been collected in the interior. However, several recent trans-basin hydrographic

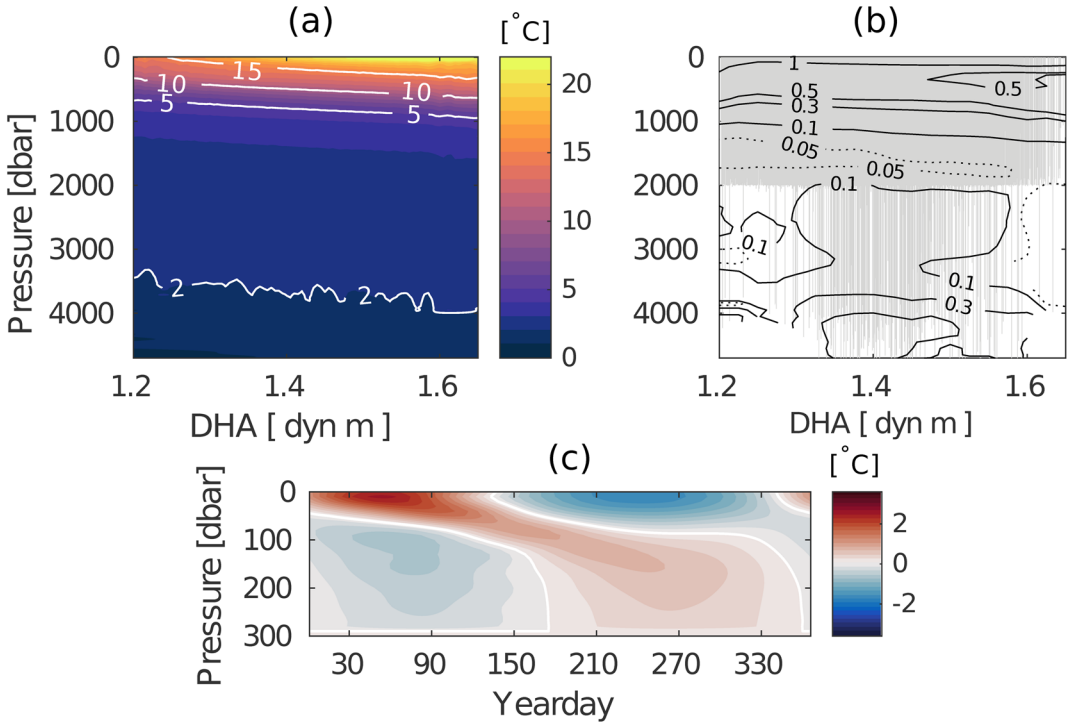

Figure 3. GEM-A field of temperature determined for the mid-ocean region. (a) GEM-A lookup table for temperature as a function of pressure and dynamic height anomalies (DHA). (b) Root-mean-square differences between the original hydrographic temperature measurements and the seasonally uncorrected GEM-A lookup table values. The solid and dotted contours represent progressively smaller contour intervals, with temperature values labeled in [°C]. The gray vertical lines show the locations (in DHA space) of the original CTD and Argo measurements. (c) Seasonal correction field applied to the GEM-A lookup table temperature values.

sections have increased data density in the central region of the South Atlantic to 482 casts, with two GO-SHIP repeat hydrographic sections sampled 1 or 3 times over the past 30 years: Section A10 along 30°S (in 1992, 2003, and 2011), and Section A10.5 along 34.5°S (in 2017). The strength of the original GEM method to derive lookup tables for temperature and salinity has always been the ability to simultaneously derive observation-based error bars for the lookup table estimates (e.g., Meinen & Watts, 2000; Watts et al., 2001). The new method presented here—termed GEM-Altimetry (GEM-A)—has the same ability. Theoretically, different vertical profiles of temperature and salinity can generate the same vertically integrated DHA (or round-trip acoustic travel time). With the GEM and GEM-A methods, we use the scatter between the original data (CTD and Argo) and the resulting smoothed lookup tables to provide a natural "accuracy estimate" for the lookup tables, and account for this potential source of error (Figure 3b). This scatter represents the true ocean variability about the lookup table fields. The root-mean-square differences between the smoothed GEM-A field and the original CTD and Argo data range from about 1°C for temperature at the surface (where seasonal variability is maximum) down to around 0.05°C–0.3°C in the deep ocean. The seasonal variability of temperature near the surface is at least partially regular in time, and so the GEM-A estimates near the surface can be improved using a seasonal correction field in the upper 300 dbar following the methods presented in Watts et al. (2001). At each pressure level, the temperature residuals were calculated between each original hydrographic data and its corresponding GEM-A profile, and these residuals were then indexed by time-of-year. The original hydrographic observations are fairly uniformly distributed throughout the year, with more than 3,500 profiles every season, so there is excellent data coverage for developing these seasonal corrections. The temperature residuals were then interpolated onto a regular grid to create a lookup table of seasonal variations (Figure 3c). These seasonal corrections were finally applied to the temperature profiles produced by the standard GEM-A lookup tables, thereby improving the GEM-A estimates in the near-surface layer (Figure 4—lower panels).

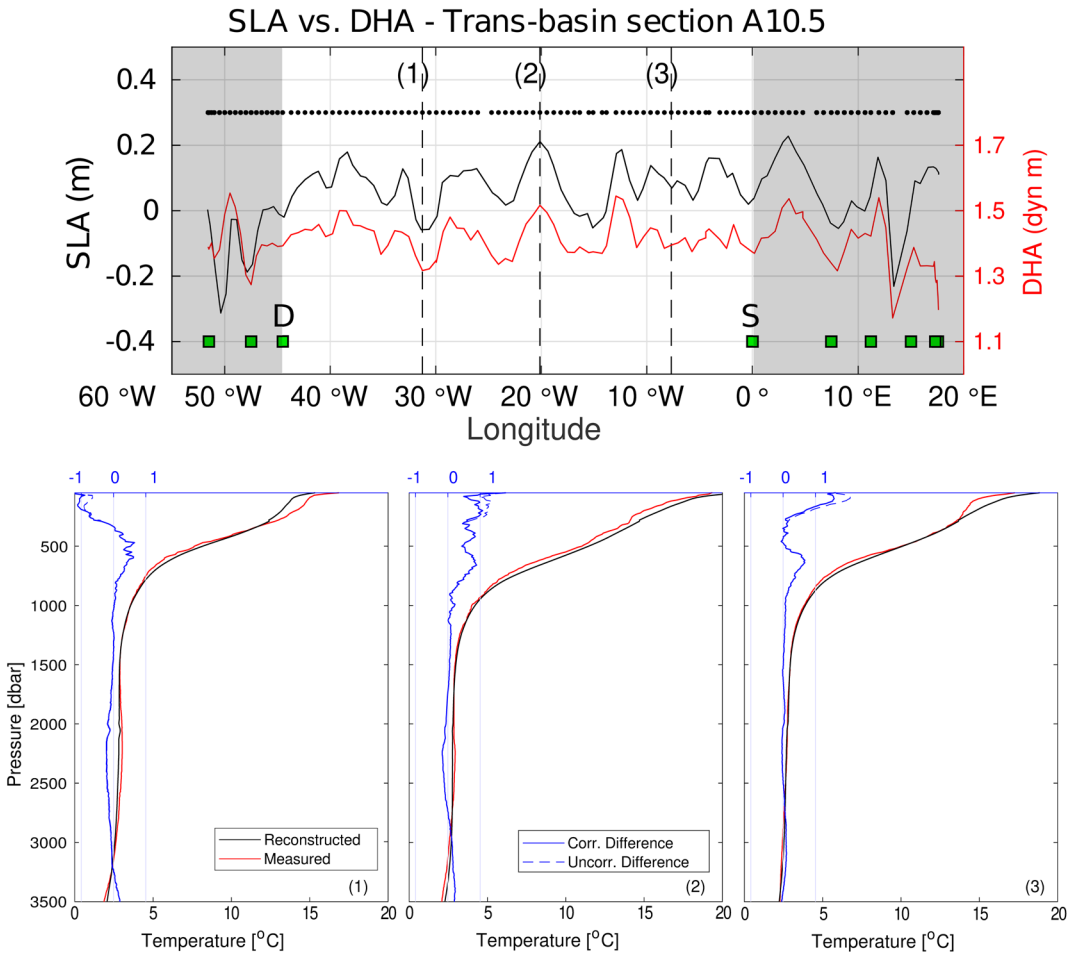

Figure 4. Application and validation of the GEM-A technique. (top) DHA calculated between the surface and 1,000 dbar from CTD temperature and salinity profiles (red line) obtained in January 2017 along 34.5°S, and concurrent sea level anomaly (SLA) measured by satellite altimeter (black line). The black dots show the locations of the hydrographic measurements. Green squares denote the positions of the PIES, with Sites D and S specifically noted with black letters. (bottom) Vertical profiles of measured (red line) and reconstructed (black line) temperature at three different stations (locations indicated with vertical dashed lines in the upper panel). The differences between the reconstructed and the measured temperature profiles are represented with the blue lines before the seasonal correction (dashed lines) and after the seasonal correction (solid lines).

Figure 4 provides an illustration of how the SLA measured by satellite altimetry was used to derive synthetic temperature profiles. Figure 4 (upper panel) shows the DHA, integrated between the surface and 1,000 dbar, from CTD temperature and salinity profiles from the hydrographic line A10.5 that was occupied in January 2017 (red line). Also shown in this panel is the concurrent in time and space (keeping in mind the effective altimetry resolutions) gridded de-seasoned SLA along the ship track obtained from the AVISO product (black line). The correlation between these two independent measurements of sea height variability across the basin is 0.45 for the entire section, but the correlation is 0.86 in the interior of the basin between the locations of Sites D and S. This comparison demonstrates that steric (baroclinic, density-driven) effects dominate SLA in the interior of the basin; and that SLA is an adequate proxy for DHA referred to 1,000 dbar far enough away from the boundaries. Synthetic temperature profiles were derived from the daily SLA transect values between Sites D and S along 34.5°S by applying the GEM-A lookup table and the seasonal correction (Figure 3). As SLA is not measured directly from the hydrographic data, SLA needs to be converted into the equivalent DHA to use the lookup table and apply the GEM-A method. The SLA were "converted" by adding the Mean Dynamic Topography (CLS18 MDT; Mulet et al., 2019). The resulting corrected time-mean SLA + MDT values were still found to be offset from hydrographically measured DHA

across the basin. As such, a further correction to the time-mean SLA trans-basin transect was determined using the difference between SLA and DHA from the World Ocean Atlas (WOA) 2018 climatology with 0.25° horizontal resolution (Locarnini et al., 2019). This time-mean correction linearly increased from 0.7 to 0.73 m, from west to east across the basin.

Once this time-invariant correction was applied, the resulting SLA + MDT + correction values were treated as equivalent to DHA, and the GEM-A lookup table and the seasonal correction were used to produce daily time series of temperature profiles at each grid point of the altimetry product between Sites D and S, similar to the GEM technique applied on the boundaries. Vertical profiles of observed and reconstructed temperature are presented at three different stations typifying low, high, and average SLA values in the basin interior to illustrate how well the GEM-A method works (Figure 4—lower panels). In this calculation, we excluded the A10.5 trans-basin section CTD profiles when we were creating the GEM-A lookup tables so that we could make a truly independent comparison of the technique. All profiles show very similar structure tracking the main thermocline and the deep structure quite well with a root-mean-squared difference smaller than 0.38°C, with the largest differences in the upper 300 dbar (Figure 4—lower panels). These observed differences are within the estimated error bars for the GEM-A lookup table (Figure 3). A similar comparison was done between the reconstructed vertical profiles of temperature (concurrent in space and time) from the PIES D and S travel time records and from the CTD of the hydrographic line A10.5 to evaluate the improvement of our new method. The PIES reconstructed temperature profile shows an upward lift of the main thermocline of about 100 m compared to the CTD data, which leads to mean square error temperature differences that are twice as large as the new GEM-A technique errors. Based on these comparisons, we are confident that altimetry data analyzed via the hydrography-derived GEM-A lookup table provide sufficient accuracy to estimate the needed interior temperature profiles for calculating MHT between Sites D and S.

2.2.2. Mean Temperature Transport Over the Shelves and in the Deep Layer

Following the same procedure as was used for the volume transport (Section 2.1.3), the ECCO2 output was used to provide a time-invariant estimate of the temperature transports on the western and eastern continental shelves/upper slopes inshore of the shallowest moorings (Q_{shelves}). The ECCO2 mean western and eastern inshore temperature transports were −0.24 PW southward and 0.01 PW northward, respectively. Evaluating the meridional flows in these relatively narrow longitude ranges with a different numerical model, like OFES, or with data from repeated trans-basin XBT transects collected along roughly the same latitude (e.g., Dong, Garzoli, Baringer, Meinen, & Goni, 2009; Garzoli, Baringer, et al., 2013), produces essentially the same estimates for these small time-mean flows (maximal differences of 0.09 PW between the different estimates; within the range of error estimates for the calculations—see Appendix for more details).

As noted above, we did not apply a mass conservation as part of our calculations, but we accounted for the unobserved temperature transport below the deepest common depths of the moorings (i.e., below 4,700 dbar) by adding a time-invariant contribution in the deep/abyssal ocean (Q_{deep}). We estimated the potential temperature values within the unobserved layer below 4,700 dbar using the WOA climatology (Figure 2b). The zonal mean potential temperature in this layer was then multiplied by the unresolved 6.6 Sv northward transport previously estimated to be transported northward below 4,700 dbar to close the mass budget (Kersalé, Meinen, et al., 2020). The resulting time-invariant estimate of the northward temperature transport in this deep layer (Q_{deep}) was 0.03 PW which is small relative to the total transport. This value, together with the shelf flows and the other terms in Equation 1 are combined together to produce daily estimates of the MHT across SAMBA.

2.2.3. Error Estimates

The error estimate (detailed in the Appendix) takes into account the accuracy of the Ekman transports, the geostrophic (relative and reference) transport estimates from the PIES, the errors that might be introduced by applying a model mean flow and temperature in the narrow continental shelf regions inshore of the shallowest moorings, and the errors that might be similarly introduced by applying a mean flow and WOA temperature below 4,700 dbar. As explained in the Appendix, those sources of error are independent of one another and are combined via a standard square root of the sum of squares method, yielding 0.3 PW as the total daily random error and 0.2 PW as the total time-mean bias error.

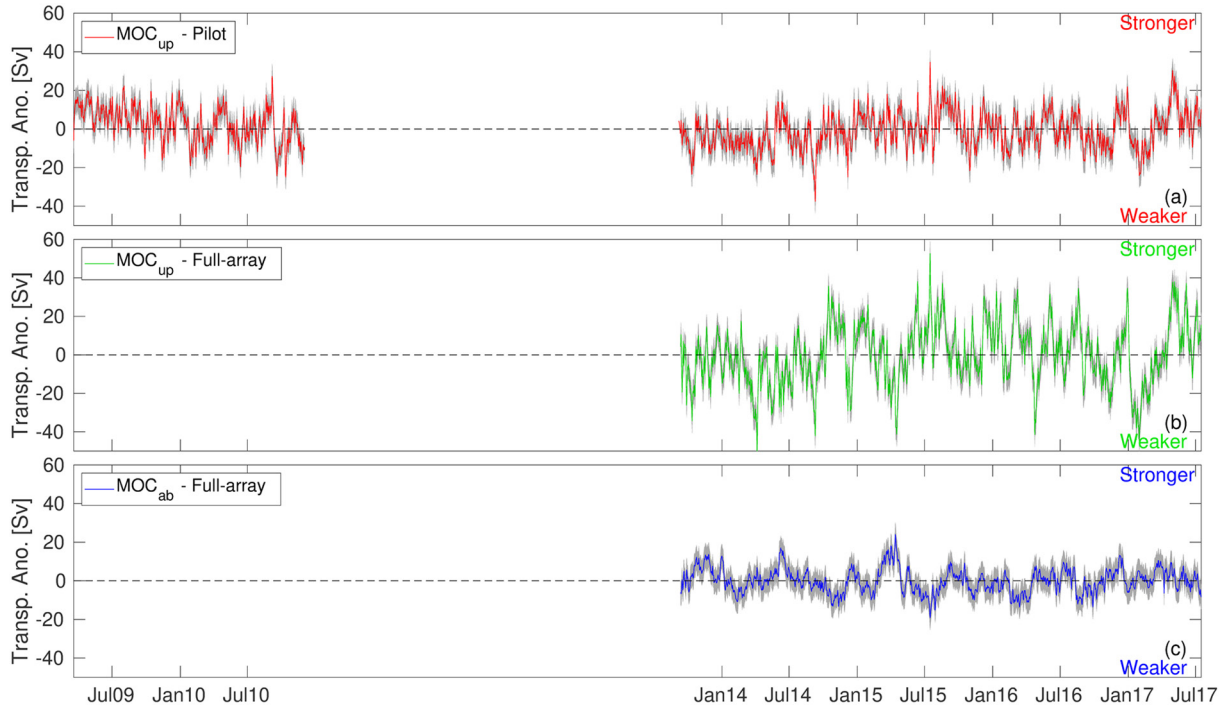

Figure 5. Temporal anomalies of the MOC volume transport: (a) for the MOC_{up} cell (defined positive northward) calculated using the pilot array configuration; (b) for the MOC_{up} cell (defined positive northward) calculated using the full array configuration; (c) for the MOC_{ab} cell (defined positive southward) calculated using the full array configuration. Gray shading indicates the estimated daily accuracy.

3. Results

3.1. MOC Variability

Kersalé, Meinen, et al. (2020) presented the resulting MOC estimates for both MOC_{up} and MOC_{ab} cells for the period September 2013 to July 2017. In this study, we present only details of the MOC results that are pertinent to the MHT results that will be discussed in latter sections, and to explore signals that were not previously discussed in Kersalé, Meinen, et al. (2020). Specifically, a careful comparison of the MOC_{up} transport calculated in the pilot (red squares in Figure 2b) and full (all squares in Figure 2b) configurations is presented here to illustrate how the MOC_{up} versus MHT covariability may allow for estimating MHT for the period March 2009–December 2010 when only the pilot array was deployed (Meinen, Speich, Perez, et al., 2013). The pilot array configuration does provide a fairly solid estimate of the MOC_{up} variability; the correlation coefficient (Thomson & Emery, 2014) between the MOC_{up} calculated over 2013–2017 using the pilot array configuration (just two end-point PIES moorings used, Figure 5a) and the estimate using the full resolution of moorings (nine PIES sites used, Figure 5b) is $r = 0.73$. The correlation coefficient calculated over the same period between the southward transport in the MOC_{ab} cell (Figure 5c) and the northward transport in the MOC_{up} cell is essentially zero when MOC_{up} is calculated using the pilot array configuration (Figure 5a), and $r \sim -0.40$ when it is calculated using the full configuration (Figure 5b). The temporal standard deviation (σ) of the daily MOC_{up} cell strength calculated over the continuous 4 years observational period with the full resolution array is equal to 15.4 Sv, highlighting the high-frequency variability at 34.5°S (Figure 5, Table 1). This daily σ exceeds the previous estimate of ~9 Sv using the pilot array configuration, and this result holds true regardless of whether or not the first 20-months of data are included in the pilot configuration calculation. Stronger variability in the full array configuration is likely due to a better representation of the barotropic variations and eddies (including Agulhas Rings) using the full array resolution. In addition to the larger σ for the full resolution array compared to the pilot array, the variations observed by the fully resolved array tend to occur over longer time periods (i.e., longer integral time scale/decorrelation time scale; e.g., Thomson & Emery, 2014) than was observed in the pilot array configuration (Table 1).

Table 1
Statistics for the Total MOC_{up} and the Ekman, Relative, and Reference Components of it (Mean Value, Standard Deviation (σ), and Integral Time Scale (i.t.s.) or Decorrelation Time Scale)

		Pilot 2009–2017	Pilot 2013–2017	Full array 2013–2017
Total	Mean	18.8 Sv	17.7 Sv	17.3 Sv
	σ	9.3 Sv	9.2 Sv	15.4 Sv (14.7 Sv)
	i.t.s.	12 days	12 days	14 days (16 days)
Ekman contribution	σ	4.4 Sv	4.2 Sv	4.2 Sv (3.9 Sv)
	i.t.s.	6 days	6 days	6 days (2 days)
Reference contribution	σ	5.0 Sv	5.1 Sv	7.1 Sv (7.0 Sv)
	i.t.s.	11 days	10 days	12 days (12 days)
Relative contribution	σ	7.2 Sv	6.8 Sv	9.9 Sv (9.4 Sv)
	i.t.s.	16 days	13 days	16 days (19 days)
Correlation with the total MOC	Ek	0.44	0.43	*0.27 (0.20)*
	Ref	0.38	0.44	0.77 (0.80)
	Rel	0.77	0.75	0.90 (0.90)

Note. All statistics are calculated for the pilot and full array configurations. Numbers in italics show correlations that are not statistically significant from zero at the 95% confidence level. Numbers in parentheses are statistics if the seasonal time scale is removed.

The strength of the method for calculating the MOC used herein is that it does not use a "residual" method to obtain the barotropic component of the flow (e.g., Kanzow, Cunningham, Rayner, et al., 2007; McCarthy, Smeed, et al., 2015). Instead, we obtained the reference (barotropic) velocity variability directly from data (bottom pressure gradients). So, it is possible to decompose the MOC variability into the variations associated with the relative (density-driven), reference (bottom pressure-driven) and Ekman (wind-driven) transport contributions. For all components, each "contribution" is estimated as the difference between the total MOC volume transport and the MOC calculated while holding one term (e.g., the Ekman transport) constant following the methods presented in Meinen, Speich, Piola, et al. (2018). Applying these methods to the fully resolved array, rather than the pilot array used by Meinen, Speich, Piola, et al. (2018), demonstrates some noticeable differences (Table 1). Although the relative (density-driven) contribution to the total MOC_{up} cell strength is highly correlated when calculated in either the pilot ($r = 0.75$) or full ($r = 0.9$) resolution configurations, the reference (bottom pressure-driven) contribution to the total MOC_{up} variability is less well correlated when calculated by the two different configurations ($r = 0.44$–0.77). This likely relates to better capturing of the barotropic flow interactions with the topography across the basin. The wind product used to compute the Ekman transport is the same for the two calculations; hence, the Ekman variability does not change (see σ in Table 1). The impact of the Ekman contribution to the total MOC_{up} cell strength, however, is weaker for the full array configuration (correlation coefficients between 0.27 and 0.43 in Table 1) as both the reference and the relative velocity contributions are more energetic. The larger variability and longer integral time scale of the MOC_{up} cell time series for the full array compared to the pilot configuration are also borne out by comparison of σ and integral time scales of the relative and reference contributions. And while the Ekman, relative, and reference contributions to the total MOC_{up} cell strength are all uncorrelated with one another when calculated using the pilot array configuration (correlations $r \leq 0.20$), the results from the full array configuration do show a low but statistically significant correlation between the relative and the reference contributions to the total MOC_{up} cell variability ($r = 0.56$, not shown). In general, however, there is moderately good agreement between the results determined using the pilot and full array configurations, which suggests that the pilot configuration does provide sufficient information to be of value to reconstruct an extended MHT time series. If the seasonal time scale is removed, these statistics generally show a decrease of the variance and an increase of the integral time scale, except for the Ekman anomaly where a decrease of the integral time scale is observed (see parentheses in the right column of Table 1). Note, that none of the correlations in Table 1 change significantly for the time series whether the seasonal cycle is removed or not.

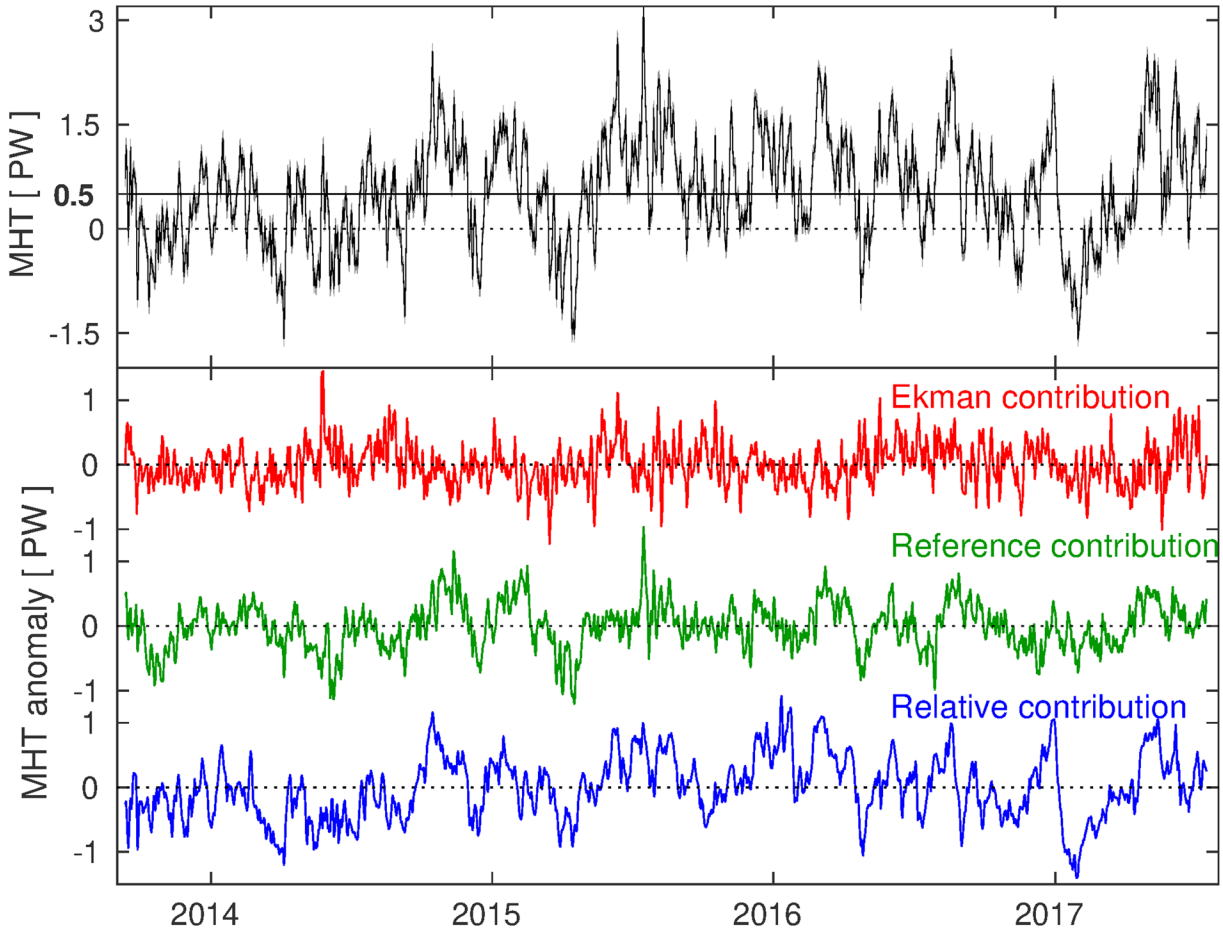

Figure 6. Temporal variability of the total MHT and its contributions. (top) MHT time series at 34.5°S (black line) with estimated daily error bars (gray shading). (bottom) The contributions of Ekman (red line), geostrophic reference flow (green line), and geostrophic relative flow (blue line) components to the MHT variability.

3.2. MHT Variability

The daily total MHT calculated as described in Section 2.2 demonstrates variability on a wide range of time scales (Figure 6, black line). The mean estimate of the MHT is 0.5 ± 0.2 PW (time-mean ± combined statistical and bias errors; see Appendix) with a standard deviation, σ, of 0.8 PW. The observed variability is large, with the peak-to-peak daily range spanning from −1.6 to 3.2 PW. There is a positive MHT trend of 0.14 PW per year over the 4-year-period, however the trend is not statistically significant from zero based on the estimated 95% confidence limit error bars (0.18 PW per year, based on the estimated integral time scale of 14 days). A longer data record will be required to confirm the robustness of this 4-year trend, should the trend continue.

The computed total MHT exhibits strong variations at time scales of a few days to a few weeks. The contributions of the MHT variability from the relative (density-driven), reference (bottom pressure-driven), and Ekman (direct wind-driven) variability can be determined in exactly the same way as was done for the MOC_{up} cell (Section 3.1). The results of this decomposition demonstrate that the total MHT variability is most strongly driven by the geostrophic relative velocity contribution to the heat transport (Figure 6—blue line; $\sigma = 0.5$ PW), with the geostrophic reference velocity (green line; $\sigma = 0.4$ PW) and the Ekman (red line; $\sigma = 0.3$ PW) contributions playing smaller but non-negligible roles. Evaluating the correlation coefficients between these various components and the total MHT indicates that geostrophic relative transport explains about 72% of the total variance ($r = 0.85$), whereas the reference contribution about 52% ($r = 0.72$) and the Ekman contribution explain about 17% ($r = 0.41$) of the total variance. All of these correlations are

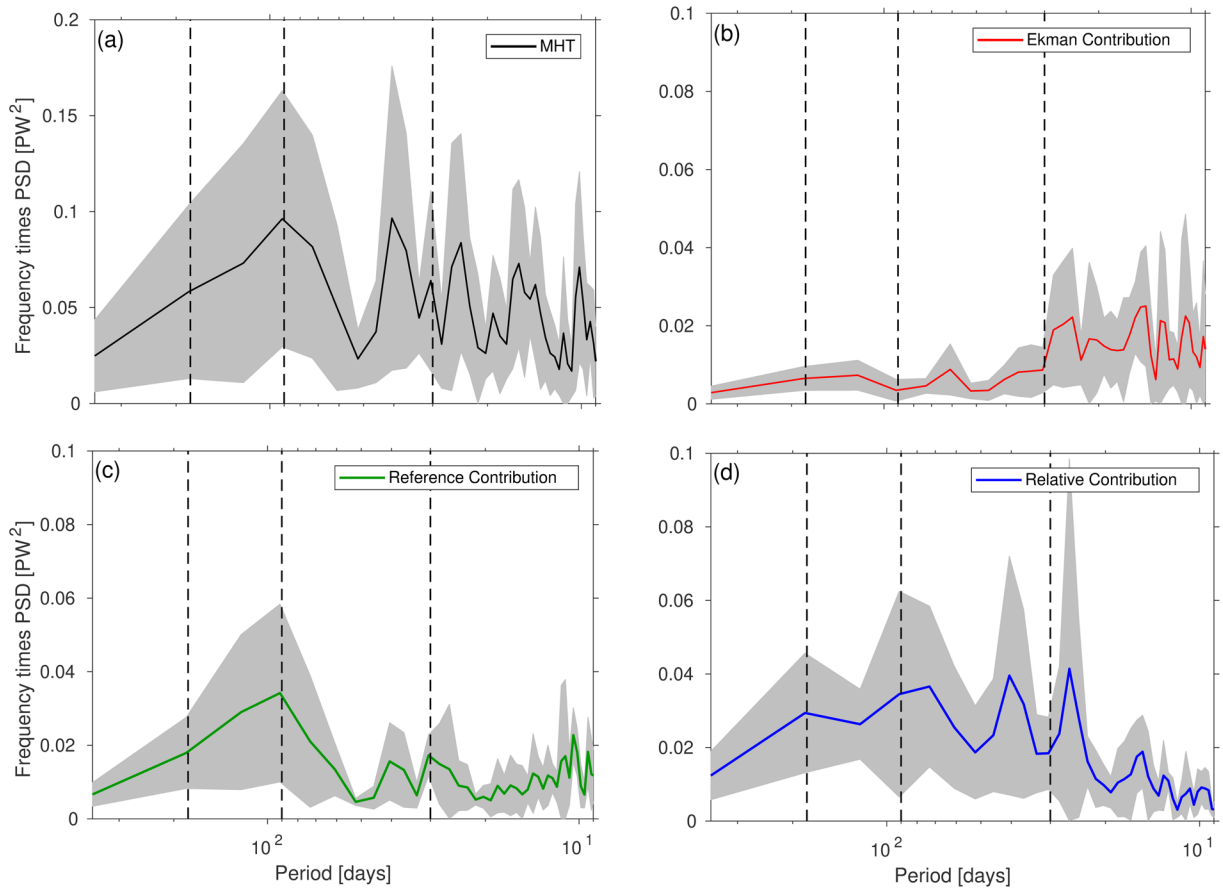

Figure 7. Variance-preserving spectra of the MHT time series. (a) The total, (b) the Ekman, (c) the geostrophic reference, and (d) the geostrophic relative transports are shown. Spectra were determined using Welch's averaged periodogram method with a 1-year window allowing 0.5 year of overlap. Gray shading areas indicate the 95% confidence limits. Vertical black dashed lines indicate the semi-annual, 3-, and 1-month periods (from left to right). Note the different *y*-axis limits for the total panel (a) versus the other panels (b, c, and d).

significantly different from zero, based on estimated integral time scales of 20, 12, and 6 days for the relative, reference, and Ekman terms, respectively. Note, that the variance percentages add up to more than 100% because there is some compensation between the terms, although only the cross-correlation between the relative and reference components is itself significantly different from zero ($r = 0.53$). None of the other MHT component terms are correlated with each other at a level that is significantly different from zero ($|r| < 0.1$). The integral time scale of 6 days for the Ekman term suggests that the directly wind-forced role in the MHT is at the higher end of the frequency spectrum as expected from the atmospheric synoptic scale variability. The reference/barotropic integral time scale being shorter than the relative/density integral time scale is consistent with expected barotropic and baroclinic wave propagation speeds, respectively (e.g., Vallis, 2017). Note that as with the MOC results presented earlier, there are no significant changes to the trends or correlation-regression analyses presented if the seasonal cycle (discussed in Section 3.5) is removed prior to the trend/correlation calculations (not shown).

The spectrum of the total MHT at 34.5°S (Figure 7a) demonstrates that there is significant energy at sub-seasonal time scales, with multiple peaks between 10- and 40-day time scales. This strong variability is likely due to the propagation of Agulhas Rings (e.g., Garzoli & Gordon, 1996), and wave signals and other phenomena observed in this same frequency band (topographic Rossby Waves; mesoscale structures; Dong, Garzoli, Baringer, Meinen, & Goni, 2009; Garzoli & Simionato, 1990). Levels of significant energy are also observed at seasonal and longer periods. These variations likely reflect both the influence of the Brazil and Benguela Currents, the Deep Western and Eastern Boundary Currents just offshore (Kersalé, Perez, et al., 2019; Meinen, Garzoli, et al., 2017; Meinen, Piola, et al., 2012), and the upwelling in the southern

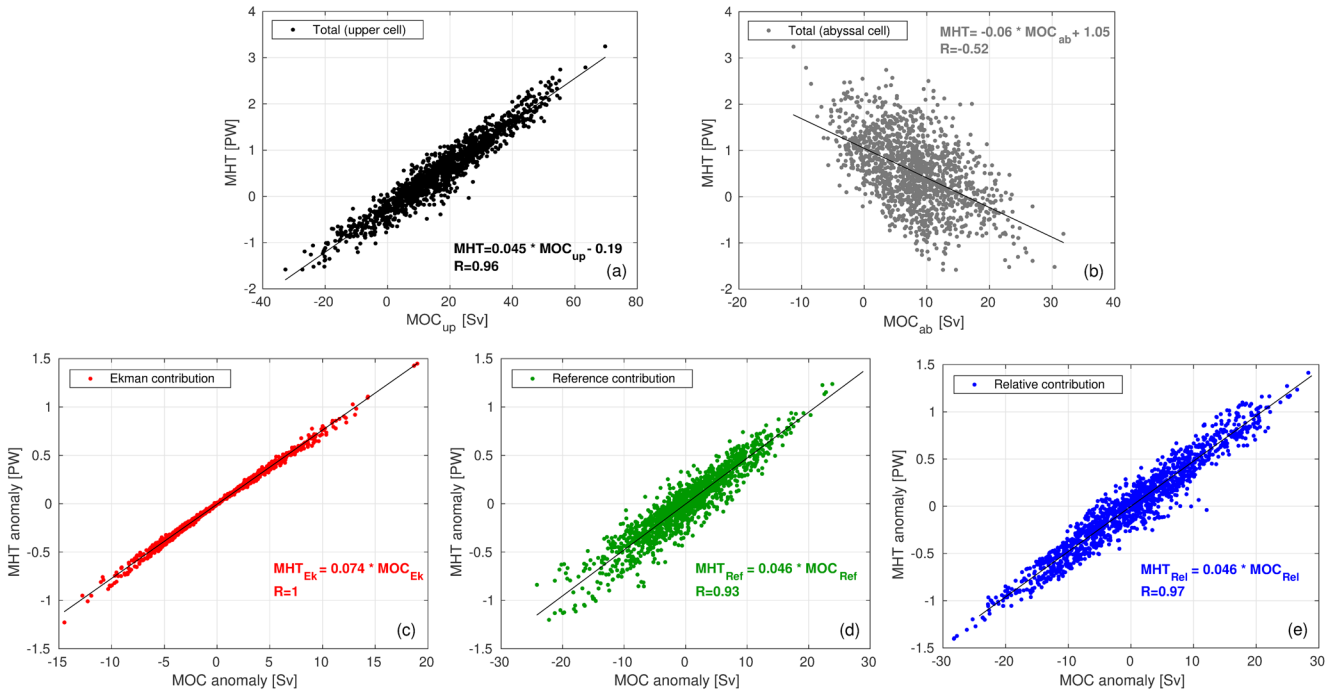

Figure 8. MHT and MOC covariability. (a) Linear relationships between MHT and the MOC_{up} cell strength and (b) the MOC_{ab} cell strength (defined positive southward) across 34.5°S from the moored instruments. (c) The relationships between the MHT and MOC_{up} anomalies are also shown for the Ekman, (d) the geostrophic reference, and (e) the geostrophic relative. The lines are the linear relations between the variables.

Benguela region (Blanke et al., 2005). It must be noted, however, that the accuracy of the spectra at time scales longer than seasonal is limited due to the relatively short 4-year length of the analyzed record. Spectra of the Ekman (Figure 7b), reference (Figure 7c), and relative (Figure 7d) contributions to the total MHT illustrate the importance of the three terms to the total MHT variability at different time scales. Spectral analysis of the Ekman term confirms its dominant role at very short periods, with high energy found in the 10–28-day band, and that it has very weak impact at periods longer than about 40 days. The geostrophic reference term exhibits energy peaks at the same periods as are observed for the total MHT for periods >30 days. At shorter periods, the geostrophic reference term spectrum exhibits noisy energy peaks between 10 and 23 days. The geostrophic relative contribution exhibits one strong peak at 40 days, which is also in the spectrum of the total MHT (and in the reference term). At shorter periods, the relative term and total MHT spectra show two dominant peaks at 15 and 24 days that are not reflected in the reference term spectrum. Levels of high energy are also observed in the relative term at intraseasonal and at semi-annual periods. The intraseasonal peak is centered at periods a bit shorter than the total MHT, but once again it must be stressed that some caution is required in interpreting the spectra at periods longer than seasonal due to the relatively short length of record, as indicated by the large error bars on the spectra.

3.3. MHT and MOC Covariability

Comparing the daily time series of the MOC_{up} cell strength (Figure 5b) and the full-depth MHT strength (Figure 6, top panel) we find that the records are highly correlated ($r = 0.96$; see also Figure 8a). The coherence spectrum calculated between the MOC_{up} cell and MHT (not shown) is a bit noisy, but aside from narrow lower significant coherence spikes at ~18, 21, and 49 days, the coherence is well above 0.8. The southward transport of the MOC_{ab} cell (Figure 5c) and the total MHT are modestly correlated ($r = -0.52$; see also Figure 8b) indicating that the variability of the MOC_{ab} volume transport explains about one-quarter of the total MHT variance (0.6 PW), which is a new result. The Ekman, reference, and relative contributions to the MOC_{up} cell strength and their corresponding contributions to the full-depth MHT are also highly correlated (Figures 8c–8e), with correlation coefficients of $r = 1$, 0.93, and 0.97, respectively.

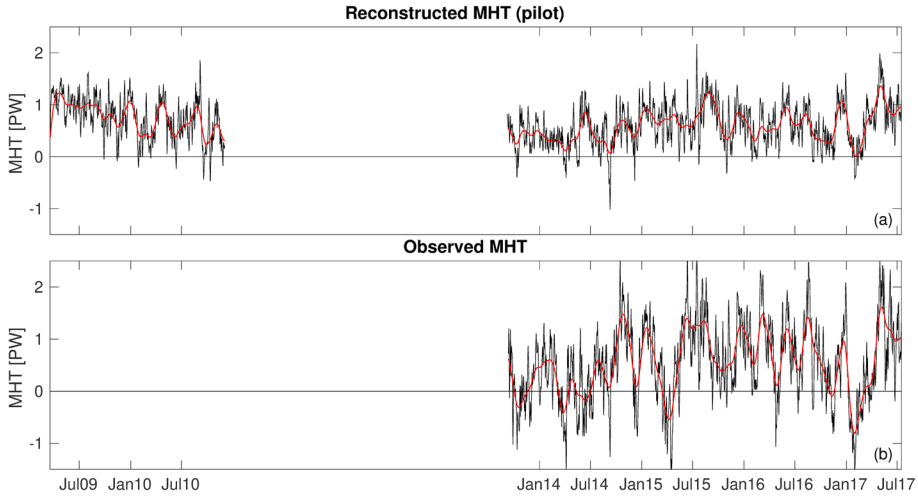

Figure 9. Toward a longer MHT time series. (a) Reconstructed MHT time series at 34.5°S for the pilot array configuration using the linear regression of the total variability. (b) MHT time series at 34.5°S from the full array configuration (same as Figure 6). The red time series are the 60-day 2nd order Butterworth low-pass filtered record.

When MHT is regressed onto the MOC_{up} strength, a robust linear relationship is found (Figure 8a) indicating that a 1 Sv increase in the MOC_{up} would increase the MHT by 0.045 ± 0.004 PW at 95% confidence limits. Note that the MHT versus MOC_{up} line does not pass through zero PW at zero Sv, suggesting that variations in MOC_{ab} can dominate the MHT changes when the MOC_{up} value is very small. If the regression is computed for the geostrophic variability only (excluding the Ekman variability, not shown) following the methodology of Johns et al. (2011), this coefficient remains within the range of error estimates. A similar result (high correlation and tight linear regression) has previously been found at 34.5°S and other latitudes from a variety of observational platforms (e.g., Dong, Garzoli, Baringer, Meinen, & Goni, 2009; Dong, Goni, & Bringas, 2015; Johns et al., 2011; Majumder et al., 2016) and from numerical ocean models (Dong, Baringer, et al., 2011; Perez et al., 2011). The sensitivity of the MHT to a change in the strength of the Ekman (Figure 8c), reference (Figure 8d) and relative (Figure 8e) contributions to the MOC_{up} are also evaluated and yield 0.074, 0.046, and 0.046 PW per Sverdrup, respectively. The relationship between the MOC_{up} cell and the MHT does not appear to have a strong time scale dependence. Although there is far more scatter in the relationship, MHT does vary linearly with the MOC_{ab} (−0.06 PW per Sverdrup of southward transport, Figure 8b). Note that when a linear regression is built that includes MOC_{up} and MOC_{ab}, the MOC_{up} linear regression coefficient is nearly the same as the coefficient when we do not include MOC_{ab}.

Using the coefficients from the linear regression of the total variability (Figure 8a), we can reconstruct an extended MHT time series for the period March 2009 to December 2010 when only the pilot version of the SAMBA mooring line was in place. In essence a linear relationship is derived between the total MOC_{up} cell strength (Figure 5b) and the full-depth MHT (Figure 9b), and this slope and intercept are then used to convert the pilot configuration estimate of the MOC_{up} cell strength (Figure 5a) into an equivalent MHT (Figure 9a). Comparing the results of this MHT reconstruction technique during the 2013–2017 period when the full SAMBA array resolution is available, a correlation coefficient between the pilot array method and the fully resolved SAMBA method is calculated as $r = 0.69$. The daily σ of the full-depth MHT (0.8 PW) exceeds the estimate of 0.4 PW using the reconstructed time series regardless of whether the first 20-months of data are included or not. As such, one can argue that the pilot array configuration can capture roughly half of the variance in the MHT for those time scales which can be observed with a 4-year-long record (i.e., daily to seasonal time scales, a longer record is needed to determine if this reconstruction has skill at reproducing interannual signals). Because we want to capture more than half of the MHT variance with our observing system, the results presented herein demonstrate the need for observing the ocean with a better resolution than the pilot array configuration provided. Nevertheless, the reconstructed time series does allow us to calculate a new estimate of the MHT trend over the full period. From 2009 to 2017, there is a weak negative MHT trend of −0.02 ± 0.05 PW per year (not statistically different from zero). While the trends determined over the full time period or the 4-year-period for both the MHT and the MOC_{up} are not

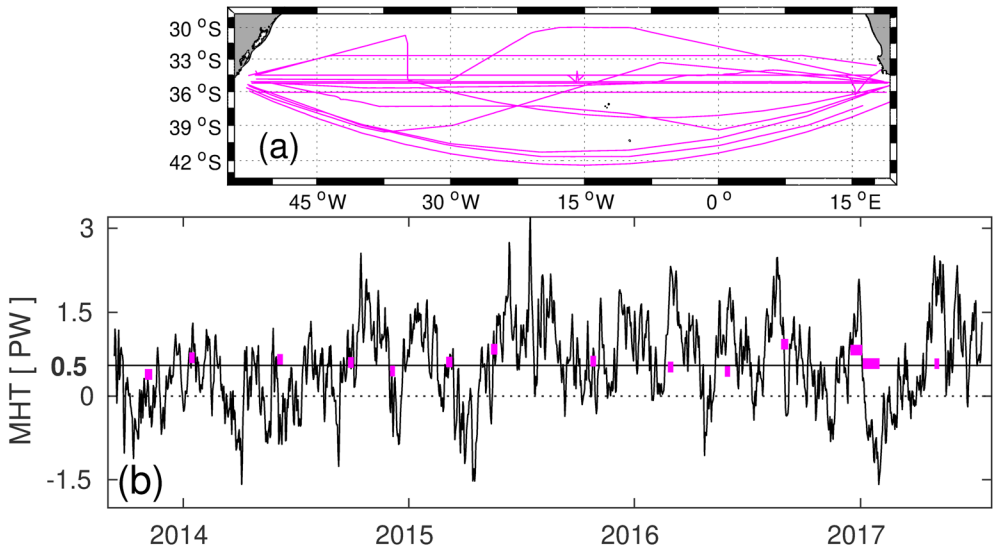

Figure 10. XBT-derived and continuous daily MHT estimates. (a) Locations of the 14 high-density XBT lines conducted in the South Atlantic during the observational time period of the moored instruments concurrent with the moored record. (b) MHT time series at 34.5°S (black line). Magenta bars represent 14 MHT estimates determined from trans-basin XBT sections where the horizontal length of the bar illustrates the start and end times of each trans-basin cruise.

significant, the negative trends within the initial ~20-month are statistically significant from zero based on the estimated error bars (MHT trend of -0.38 ± 0.28 PW/year and MOC_{up} trend of -8.5 ± 6.4 Sv/year at 95% confidence limits). Since it is only a ~20-month record, the trends over this period may simply be a reflection of interannual variations which we cannot properly resolve due to the relatively short length of records. Nevertheless, comparing the evolution of MHT from the two records, we see that MHT starts above 1 PW in 2009 and becomes negative in 2010, then steadily rebounds from 2013 to 2017 back to values well above 0.5 PW, pointing to interannual modulation in the strength of MHT at 34.5°S. These shifts in MHT are consistent with the shifts observed in MOC_{up} by Meinen, Speich, Piola, et al. (2018).

3.4. Comparison With Other Data

A critical step when developing a new method for estimating a nonlinear quantity, such as MHT, is validating the results against prior estimates. Having said that, this is a challenging task in the South Atlantic due to the limited contemporaneous measurements in the region. The only purely in situ data set available for comparison to the daily time-varying MHT from SAMBA at 34.5°S comes from repeated XBT transects collected nominally along the same latitude line (AX18) roughly every 3 months (e.g., Dong, Garzoli, Baringer, Meinen, & Goni, 2009; Garzoli & Baringer, 2007; Garzoli, Baringer, et al., 2013; Figure 10a). Updating the XBT records using data from more recent transects collected since those earlier articles were published, there are 14 independent XBT transects that are concurrent with the SAMBA record during 2013–2017. The XBT-derived MHT values show some agreement with the daily SAMBA MHT time series, with the XBT transect observations overlapping with the continuous daily time series at least at one point during the time period of each transect for most of the XBT transects (Figure 10b, magenta bars). Averaging the SAMBA data subsampled during the period spanned by each XBT transect realization (not shown), the root-mean-squared difference between the individual XBT values and the concurrent SAMBA values is quite large (0.67 PW). However, the time-mean MHT values derived from XBT during 2013–2017 and from the moored instruments subsampled over the same period agree pretty well—within 5% of the mean value itself (mean values of 0.62 and 0.67 PW, for the XBT and subsampled SAMBA moorings data, respectively), suggesting that the quarterly XBT sections can robustly determine the 4-year mean (without significant aliasing).

The variability exhibited in the continuous time series of MHT during the one to 4-week period of each XBT section is quite significant, with the daily σ varying between 0.14 and 0.68 PW when calculated during time

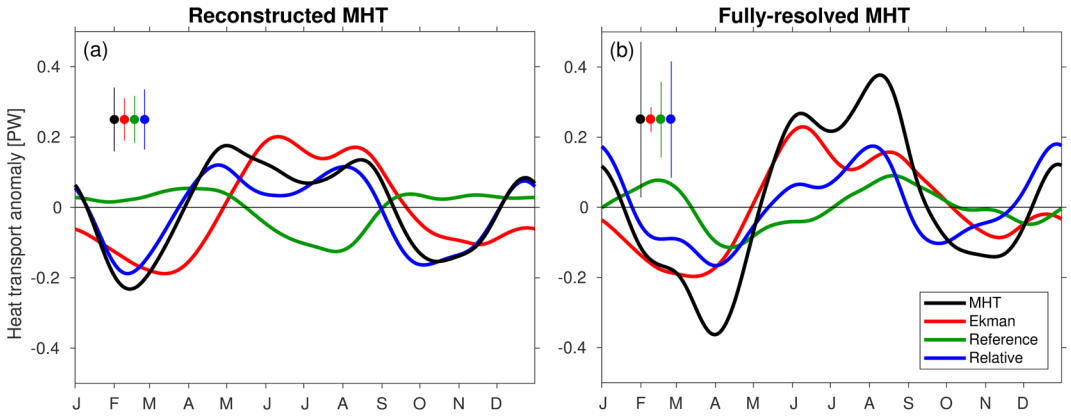

Figure 11. Seasonal anomalies of the MHT and its contributions. Seasonal anomaly of the reconstructed MHT (a; Figure 9a) and the fully resolved MHT (b; Figure 9b) time series over the 6 and 4 years observational period, respectively. The seasonal anomaly of the total, geostrophic relative, geostrophic reference, and Ekman transports are shown. Error bars indicated in the upper left represent ±1 standard error, with colors matching the corresponding time series.

windows of the different XBT transect realizations (not shown). These large temporal variations illustrate the asynopticity issues that are inherent in collecting trans-basin hydrographic sections of high-frequency signals such as MHT and the importance of daily temporal resolution to avoid aliasing of highly energetic short period variations. It is impossible using observations to determine precisely how much of the difference between the XBT heat transport estimates and the moored instruments MHT averaged during the XBT sections can be explained due to asynoptic errors or latitudinal sampling differences.

3.5. Seasonal Variability

Although we get a hint of interannual variations that might influence MHT from the reconstructed time series using the pilot configuration (Figure 9a), the longest robust time scale of variability that can be evaluated using the SAMBA data so far is probably a seasonal cycle. The seasonal cycle in the reconstructed MHT from SAMBA for the pilot array configuration shows a semi-annual period (Figure 11a—black line), with maxima in transport during May to September and during December to January. This result is consistent with the previously published MOC_{up} cell seasonal cycles captured by the pilot configuration (Meinen, Speich, Piola, et al., 2018). The associated seasonal cycle in the best-quality fully resolved total MHT (Figure 9b) from SAMBA during 2013–2017 (Figure 11b—black line) is consistent with the MOC_{up} cell seasonal cycle captured by the full array configuration (Kersalé, Meinen, et al., 2020) with a stronger maximum in transport over a shorter time period (from July to September) compared to the pilot study. The seasonality of the MHT component associated with the Ekman transport for both configurations (Figure 11—red lines) is annual and is fairly consistent in both amplitude and phase with the Ekman component of the MHT that has previously been estimated from the repeated AX18 XBT transects (e.g., Garzoli, Baringer, et al., 2013). The geostrophic relative velocity terms (Figure 11b—blue lines) clearly have a semi-annual component to it and agree in phase with the corresponding total MHT variability. This consistency between geostrophic relative term and total seasonal cycles is also similar to what has previously been observed for the MOC_{up} cell (e.g., Meinen, Speich, Piola, et al., 2018). The seasonal cycle of the reference term (Figure 11b—green line) also has something of a semi-annual period to it, with 2 months of positive anomalies in February/March that are roughly 180° out of phase with the annual seasonal cycle in the Ekman term. This near compensation is not maintained for the rest of the year, where the reference term becomes in phase, albeit with a ~1-month time-lag, with the other terms. Interestingly, the reference MHT annual cycle is a bit different than the reference MOC_{up} annual cycle of the full record calculated for the pilot configuration (Meinen, Speich, Piola, et al., 2018) or the reconstructed reference MHT annual cycle (Figure 11a), suggesting that the pilot configuration may be somehow missing important barotropic contributions to the seasonal cycle. With only 4 years of data for the fully resolved total MHT, however, this result must be viewed with caution, and should be revisited again in the future when additional years of data are available.

The total MHT seasonal cycle found here is quite different from what has been observed by prior studies of the MHT variability at this latitude using XBT transect data (e.g., Dong, Garzoli, Baringer, Meinen, & Goni, 2009; Garzoli, Baringer, et al., 2013). Those earlier studies, which did not measure the barotropic/reference term and instead estimated it as a residual, found an annual cycle of the Ekman component that was roughly 180° out of phase with, and of the same order of magnitude as, the geostrophic/relative component (Dong, Garzoli, Baringer, Meinen, & Goni, 2009; Garzoli & Baringer, 2007). As a consequence, the observed annual cycle of the total (Ekman plus geostrophic/relative) MHT estimated by those earlier studies is almost zero. Prior numerical model studies of the South Atlantic, by contrast, have found a significant MHT annual cycle at this location, although the models tended to have annual MHT cycles that very closely followed that of the Ekman flow with almost no geostrophic seasonality (Baringer & Garzoli, 2007; Dong, Baringer, et al., 2011; Perez et al., 2011).

An important conclusion to be drawn from the results presented herein, is that there is significant seasonal variability in all three components of the MHT (Ekman, baroclinic/relative, barotropic/reference), and that the seasonal variation of the MHT is due to the combination of all terms. The true seasonal cycle in MHT is not dominated only by Ekman heat transport variability, as has frequently been implied by modeling studies, and the barotropic/reference seasonality, which has not been observed in most previous ship section estimates of the MHT, is significant and independent of the other terms.

4. Summary and Conclusions

The observations and the methodology described in this study provide daily continuous time series of volume and heat transports, which are jointly analyzed for the first time at the key location for inter-ocean exchange in the South Atlantic. The PIES instruments from SAMBA provide daily information on the variability of the South Atlantic upper and abyssal MOC volume transport, via geostrophic velocity inferred from widely spaced moorings. The PIES capture the MOC well, but alone they are not sufficient to estimate MHT in the largely unsampled basin interior. In order to construct suitably accurate estimates of zonally averaged temperature profiles in the interior concurrent with the geostrophic velocities, the enhanced spatial resolution of SLA and available hydrographic data are used to create empirical lookup tables relating temperature to pressure and SLA (i.e., the new GEM-A method). Zonally integrated geostrophic flow is combined with these derived temperature profiles to obtain a new daily South Atlantic MHT time series estimate. This methodology is applicable at other latitudes than 34.5°S, or other basins, where the boundary transports are well resolved by moored arrays but the interior is sparsely observed. The main conclusions from this study are as follows:

- The mean MHT across 34.5°S for the 2013–2017 period of observations is 0.5 ± 0.2 PW. This mean value is consistent with repeated XBT transects collected along the same latitude line with the same uncertainty (AX18, Garzoli, Baringer, et al., 2013)
- The short-term variability of the heat transport is large, with a peak-to-peak range of 4.6 PW and standard deviation of 0.8 PW. The geostrophic relative velocity contribution appears to play a larger role to the total MHT variability, but the geostrophic reference transport changes have also a non-trivial role at different time scales. Further analyses should be done to link the variability contained in geostrophic circulation to external forcing (e.g., wind-driven baroclinic variability, Rossby waves) and/or internal variability (e.g., mesoscale eddies, frontal meanders)
- MHT is highly correlated with changes in the strength of the MOC upper cell, and modestly anti-correlated with changes in the strength of the southward volume transport in the MOC abyssal cell
- An empirical relationship is developed that allows for the reconstruction of a longer MHT time series using the MOC upper cell transport computed from the 2009–2010 pilot array. The comparison of the reconstructed MHT and the fully resolved MHT shows that the pilot array configuration can capture roughly half of the variance in the MHT from daily to seasonal time scales. A drop in the variability for the reconstructed time series compared to the fully resolved MHT is also observed, stressing the need for observing the ocean with a better resolution than the pilot array configuration
- For this reconstructed time series, no significant trend to the MHT record is found over the full 2009–2017 period or the 2013–2017 period, but a significant negative trend is estimated over the first pilot array period. Since it is only a ~20-month record, the trend over this period is mostly due to interannual

variability. A longer data record will be required to confirm the robustness of these trends. These results are not sensitive to whether the seasonal cycle is removed or not

- A seasonal cycle with a semi-annual period is evident, with a maximum equatorward heat transport in July to September and December to January. With significant seasonal variability in all components of the MHT, the seasonal variation of the MHT is due to the combination of all terms (baroclinic, barotropic, and Ekman)

With this study, we have refined the estimation of the MOC, its variability, and associated heat transport in the South Atlantic. With overturning arrays now at several latitudes in the Atlantic and associated growing time series, this data will greatly aid studies on meridional coherence, gyre connectivity, and ultimately teleconnections with other ocean basins. This study not only increases the value of existing elements of international observing networks, but provides the community a reference point for oceanic heat convergence studies and, hence, air-sea heat exchanges, and regional (including coastal) sea level research and prediction.

Appendix: Transport Accuracy Estimates

MOC Random and Potential Bias Measurement Error

The volume transport accuracy estimates have been calculated for the entire time period (2013–2017) that is discussed in the study of Kersalé, Meinen, et al. (2020) following the methods described within the appendix of Meinen, Speich, Perez, et al. (2013). The sources of error in the transport were separated as random or biases. The sources of random daily errors are assumed to be independent of one another, so they can also be combined via a square root of the sum of squares method, yielding 6.4 and 6.3 Sv as the total random errors in the daily MOC_{up} cell and MOC_{ab} cell volume transport estimates, respectively. When all of the sources of bias are combined, we find a total error of 5.0 and 2.7 Sv in the time-mean MOC_{up} and MOC_{ab} transports, respectively. Given the low temperature variability at depth, we will use the errors of the MOC_{up} cell volume transport for the MHT accuracy estimates. These errors will be used separately for the uncertainties associated with geostrophic velocity (or transport) relative to an assumed level of no motion (5.1 Sv—random; 5.0 Sv—bias), the Ekman transport (1.4 Sv—random; 0.02 Sv—bias), and the unmeasured transport by flows on the shallow continental shelves and upper slopes (3.5 Sv—random; 0.2 Sv—bias).

MHT Error Sensitivities to Volume Transport Components

The MHT error sensitivities are calculated within the code by propagating an error of 1 Sv through the calculation for each transport component (geostrophic transport, Ekman transport, and the shelf transport). Following the methodology of Johns et al. (2011), the 1 Sv error is distributed linearly over the top 1,000 m. The resulting error sensitivities are: Geostrophic transport: 0.04 PW/Sv, Ekman transport: 0.08 PW/Sv, and shelf transport: 0.03 PW/Sv. Measurement uncertainty associated with reasonable temperature errors in any of these components is negligible compared to the transport related errors (one order of magnitude lower).

MHT Random Measurement Error

To estimate the MHT random daily measurement uncertainty we assign the errors in the MOC transport components described previously to these MHT error sensitivities. We obtain associated MHT measurement uncertainties of 0.20, 0.11, and 0.11 PW, for the geostrophic, Ekman, and shelf transports, respectively. The additional error that might have been introduced by applying a mean flow below 4,700 dbar is estimated using the mean and standard deviation of the northward transport as the mean transport in this small deep layer (Kersalé, Meinen, et al., 2020). The resulting error estimate is equal to 0.09 PW. Those sources of errors that are independent of one another are combined via a standard square root of the sum of squares method to yield a net daily MHT uncertainty of 0.3 PW.

MHT Mean Error

Following the same approach, we use the estimated bias errors in the volume transport components described previously in the MOC error and combine these with the calculated error sensitivities. The resulting MHT bias errors are 0.20, 0.002, and 0.006 PW for the geostrophic, Ekman, and shelf transports respectively. The accuracy of the mean flow below 4,700 dbar is 2.7 Sv (Kersalé, Meinen, et al., 2020), leading to

an additional MHT bias of 0.01 PW. To these bias errors resulting from the measurements themselves, to get a total error estimate for the time-mean, we must add the statistical uncertainty. The standard error of the mean MHT estimate is equal to 0.11 PW, based on the observed standard deviation and the estimated integral time scale of 14 days. By combining the statistical and measurement bias errors randomly, the total uncertainty of the mean MHT estimate is equal to 0.23 PW.

Data Availability Statement

The CCMP version 2.0 wind product was created by Remote Sensing Systems and is made available on the web at www.remss.com. SLA satellite gridded data are available through the CMEMS website (http://marine.copernicus.eu/). MDT_CNES- CLS was produced by CLS and distributed by Aviso+, with support from Cnes (https://www.aviso.altimetry.fr/). ECCO2 output is available at: https://ecco.jpl.nasa.gov/. The data used herein from the South Atlantic MOC Basin-wide Array (SAMBA) can be found at: www.aoml.noaa.gov/phod/SAMOC_international/index.php.

Acknowledgments
The authors would like to express our great appreciation to the captains, officers, and crews of the research vessels who have supported our work. The authors are also very grateful to the support and technical staff who have helped collect and process the data presented herein, particularly R. F. Garcia who processed all of the PIES data. The authors also thank H. Lopez and two anonymous reviewers for helpful comments that improved earlier versions of this study.

References

Ansorge, I. J., Baringer, M. O., Campos, E. J. D., Dong, S., Fine, R. A., Garzoli, S. L., et al. (2014). Basin-wide oceanographic array bridges the South Atlantic. *Eos, Transactions American Geophysical Union*, *95*(6), 53–54. https://doi.org/10.1002/2014eo060001

Ballarotta, M., Ubelmann, C., Pujol, M.-I., Taburet, G., Fournier, F., Legeais, J.-F., et al. (2019). On the resolutions of ocean altimetry maps. *Ocean Science*, *15*(4), 1091–1109. https://doi.org/10.5194/os-15-1091-2019

Baringer, M. O., & Garzoli, S. L. (2007). Meridional heat transport determined with expendable bathythermographs—Part I: Error estimates from model and hydrographic data. *Deep Sea Research Part I: Oceanographic Research Papers*, *54*(8), 1390–1401. https://doi.org/10.1016/j.dsr.2007.03.011

Blanke, B., Speich, S., Bentamy, A., Roy, C., & Sow, B. (2005). Modeling the structure and variability of the southern Benguela upwelling using QuikSCAT wind forcing. *Journal of Geophysical Research*, *110*(C7), C07018. https://doi.org/10.1029/2004JC002529

Bower, A., Lozier, S., Biastoch, A., Drouin, K., Foukal, N., Furey, H., et al. (2019). Lagrangian views of the pathways of the Atlantic meridional overturning circulation. *Journal of Geophysical Research: Oceans*, *124*(8), 5313–5335. https://doi.org/10.1029/2019jc015014

Bryden, H. L., King, B. A., & McCarthy, G. D. (2011). South Atlantic overturning circulation at 24°S. *Journal of Marine Research*, *69*(1), 39–56. https://doi.org/10.1357/002224011798147633

Byrne, D. A. (2000). *From the Agulhas to the South Atlantic: Measuring inter-ocean fluxes* (Ph.D. dissertation, p. 162). Columbia University.

Cessi, P. (2019). The global overturning circulation. *Annual Review of Marine Science*, *11*, 249–270. https://doi.org/10.1146/annurev-marine-010318-095241

Cheng, L., Trenberth, K. E., Fasullo, J., Boyer, T., Abraham, J., & Zhu, J. (2017). Improved estimates of ocean heat content from 1960 to 2015. *Science Advances*, *3*(3), e1601545. https://doi.org/10.1126/sciadv.1601545

Coles, V. J., McCartney, M. S., Olson, D. B., & Smethie, W. M. (1996). Changes in Antarctic bottom water properties in the western South Atlantic in the late 1980s. *Journal of Geophysical Research*, *101*(C4), 8957–8970. https://doi.org/10.1029/95JC03721

de las Heras, M. M., & Schlitzer, R. (1999). On the importance of intermediate water flows for the global ocean overturning. *Journal of Geophysical Research*, *104*(C7), 15515–15536. https://doi.org/10.1029/1999jc900102

de Ruijter, W. P. M., Biastoch, A., Drijfhout, S. S., Lutjeharms, J. R. E., Matano, R. P., Pichevin, T., et al. (1999). Indian-Atlantic interocean exchange: Dynamics, estimation and impact. *Journal of Geophysical Research*, *104*(C9), 20885–20910. https://doi.org/10.1029/1998JC900099

Dong, S., Baringer, M. O., Goni, G. J., & Garzoli, S. L. (2011a). Importance of the assimilation of Argo float measurements on the meridional overturning circulation in the South Atlantic. *Geophysical Research Letters*, *38*(18), L18603. https://doi.org/10.1029/2011gl048982

Dong, S., Garzoli, S., & Baringer, M. (2011b). The role of interocean exchanges on decadal variations of the meridional heat transport in the South Atlantic. *Journal of Physical Oceanography*, *41*(8), 1498–1511. https://doi.org/10.1175/2011jpo4549.1

Dong, S., Garzoli, S. L., Baringer, M. O., Meinen, C. S., & Goni, G. J. (2009). Interannual variations in the Atlantic meridional overturning circulation and its relationship with the net northward heat transport in the South Atlantic. *Geophysical Research Letters*, *36*(20), L20606. https://doi.org/10.1029/2009gl039356

Dong, S., Goni, G., & Bringas, F. (2015). Temporal variability of the South Atlantic meridional overturning circulation between 20°S and 35°S. *Geophysical Research Letters*, *42*(18), 7655–7662. https://doi.org/10.1002/2015gl065603

Donohue, K. A., Watts, D. R., Tracey, K. L., Greene, A. D., & Kennelly, M. (2010). Mapping circulation in the Kuroshio Extension with an array of current and pressure recording inverted echo sounders. *Journal of Atmospheric and Oceanic Technology*, *27*(3), 507–527. https://doi.org/10.1175/2009jtecho686.1

Frajka-Williams, E., Ansorge, I. J., Baehr, J., Bryden, H. L., Chidichimo, M. P., Cunningham, S. A., et al. (2019). Atlantic meridional overturning circulation: Observed transport and variability. *Frontiers in Marine Science*, *6*, 260. https://doi.org/10.3389/fmars.2019.00260

Frajka-Williams, E., Cunningham, S. A., Bryden, H., & King, B. A. (2011). Variability of Antarctic bottom water at 24.5°N in the Atlantic. *Journal of Geophysical Research*, *116*(C11), C11026. https://doi.org/10.1029/2011JC007168

Ganachaud, A., & Wunsch, C. (2000). Improved estimates of global ocean circulation, heat transport and mixing from hydrographic data. *Nature*, *408*(6811), 453–457. https://doi.org/10.1038/35044048

Ganachaud, A., & Wunsch, C. (2003). Large-scale ocean heat and freshwater transports during the World Ocean Circulation Experiment. *Journal of Climate*, *16*(4), 696–705. https://doi.org/10.1175/1520-0442(2003)016<0696:lsohaf>2.0.co;2

Garzoli, S. L., & Baringer, M. O. (2007). Meridional heat transport determined with expandable bathythermographs—Part II: South Atlantic transport. *Deep Sea Research Part I: Oceanographic Research Papers*, *54*(8), 1402–1420. https://doi.org/10.1016/j.dsr.2007.04.013

Garzoli, S. L., Baringer, M. O., Dong, S., Perez, R. C., & Yao, Q. (2013). South Atlantic meridional fluxes. *Deep Sea Research Part I: Oceanographic Research Papers*, *71*, 21–32. https://doi.org/10.1016/j.dsr.2012.09.003

Garzoli, S. L., Dong, S., Fine, R., Meinen, C. S., Perez, R. C., Schmid, C., et al. (2015). The fate of the deep western boundary current in the South Atlantic. *Deep Sea Research Part I: Oceanographic Research Papers*, *103*, 125–136. https://doi.org/10.1016/j.dsr.2015.05.008

Garzoli, S. L., & Gordon, A. L. (1996). Origins and variability of the Benguela current. *Journal of Geophysical Research*, *101*(C1), 897–906. https://doi.org/10.1029/95JC03221

Garzoli, S. L., & Matano, R. (2011). The South Atlantic and the Atlantic meridional overturning circulation. *Deep Sea Research Part II: Topical Studies in Oceanography*, *58*(17–18), 1837–1847. https://doi.org/10.1016/j.dsr2.2010.10.063

Garzoli, S., & Simionato, C. (1990). Baroclinic instabilities and forced oscillations in the Brazil/Malvinas confluence front. *Deep Sea Research Part A. Oceanographic Research Papers*, *37*(6), 1053–1074. https://doi.org/10.1016/0198-0149(90)90110-h

Hernández-Guerra, A., Talley, L. D., Pelegrí, J. L., Vélez-Belchí, P., Baringer, M. O., Macdonald, A. M., & McDonagh, E. L. (2019). The upper, deep, abyssal and overturning circulation in the Atlantic Ocean at 30°S in 2003 and 2011. *Progress in Oceanography*, *176*, 102136. https://doi.org/10.1016/j.pocean.2019.102136

Herrford, J., Brandt, P., Kanzow, T., Hummels, R., Araujo, M., & Durgadoo, J. V. (2021). Seasonal variability of the Atlantic meridional overturning circulation at 11° S inferred from bottom pressure measurements. *Ocean Science*, *17*(1), 265–284. https://doi.org/10.5194/os-17-265-2021

Hummels, R., Brandt, P., Dengler, M., Fischer, J., Araujo, M., Veleda, D., & Durgadoo, J. V. (2015). Interannual to decadal changes in the western boundary circulation in the Atlantic at 11°S. *Geophysical Research Letters*, *42*(18), 7615–7622. https://doi.org/10.1002/2015gl065254

Johnson, G. C., & Lyman, J. M. (2020). Warming trends increasingly dominate global ocean. *Nature Climate Change*, *10*(8), 757–761. https://doi.org/10.1038/s41558-020-0822-0

Johns, W. E., Baringer, M. O., Beal, L. M., Cunningham, S. A., Kanzow, T., Bryden, H. L., et al. (2011). Continuous, array-based estimates of Atlantic Ocean heat transport at 26.5°N. *Journal of Climate*, *24*(10), 2429–2449. https://doi.org/10.1175/2010JCLI3997.1

Kanzow, T., Cunningham, S. A., Johns, W. E., Hirschi, J. J.-M., Marotzke, J., Baringer, M. O., et al. (2010). Seasonal variability of the Atlantic meridional overturning circulation at 26.5°N. *Journal of Climate*, *23*(21), 5678–5698. https://doi.org/10.1175/2010jcli3389.1

Kanzow, T., Cunningham, S. A., Rayner, D., Hirschi, J. J.-M., Johns, W. E., Baringer, M. O., et al. (2007). Observed flow compensation associated with the MOC at 26.5°N in the Atlantic. *Science*, *317*(5840), 938–941. https://doi.org/10.1126/science.1141293

Kersalé, M., Lamont, T., Speich, S., Terre, T., Laxenaire, R., Roberts, M. J., et al. (2018). Moored observations of mesoscale features in the Cape Basin: Characteristics and local impacts on water mass distributions. *Ocean Science*, *14*(5), 923–945. https://doi.org/10.5194/os-14-923-2018

Kersalé, M., Meinen, C. S., Perez, R. C., Le Hénaff, M., Valla, D., Lamont, T., et al. (2020). Highly Variable Upper and Abyssal Overturning Cells in the South Atlantic. *Science Advances*, *6*(32), eaba7573. https://doi.org/10.1126/sciadv.aba7573

Kersalé, M., Perez, R. C., Speich, S., Meinen, C. S., Lamont, T., Le Hénaff, M., et al. (2019). Shallow and deep eastern boundary currents in the South Atlantic at 34.5°S: Mean structure and variability. *Journal of Geophysical Research: Oceans*, *124*(3), 1634–1659. https://doi.org/10.1029/2018JC014554

Kopte, R., Brandt, P., Dengler, M., Tchipalanga, P. C. M., Macuéria, M., & Ostrowski, M. (2017). The Angola Current: Flow and hydrographic characteristics as observed at 11°S. *Journal of Geophysical Research: Oceans*, *122*(2), 1177–1189. https://doi.org/10.1002/2016jc012374

Lavin, A., Bryden, H. L., & Parilla, G. (1998). Meridional transport and heat flux variations in the subtropical North Atlantic. *The Global Atmosphere and Ocean System*, *6*(3), 269–293.

Lee, S.-K., Park, W., van Sebille, E., Baringer, M. O., Wang, C., Enfield, D. B., et al. (2011). What caused the significant increase in Atlantic Ocean heat content since the mid-20th century? *Geophysical Research Letters*, *38*(17), L17607. https://doi.org/10.1029/2011gl048856

Levitus, S., Antonov, J. I., Boyer, T. P., Baranova, O. K., Garcia, H. E., Locarnini, R. A., et al. (2012). World ocean heat content and thermosteric sea level change (0–2000 m), 1955–2010. *Geophysical Research Letters*, *39*(10), L10603. https://doi.org/10.1029/2012gl051106

Locarnini, R. A., Mishonov, A. V., Baranova, O. K., Boyer, T. P., Zweng, M. M., Garcia, H. E., et al. (2019). World Ocean Atlas 2018, Volume 1: Temperature. In A. Mishonov (Ed.), *NOAA Atlas NESDIS 81* (p. 52).

Lopez, H., Dong, S., Lee, S.-K., & Goni, G. (2016). Decadal modulations of interhemispheric global atmospheric circulations and monsoons by the South Atlantic meridional overturning circulation. *Journal of Climate*, *29*(5), 1831–1851. https://doi.org/10.1175/jcli-d-15-0491.1

Lumpkin, R., & Speer, K. (2007). Global ocean meridional overturning. *Journal of Physical Oceanography*, *37*(10), 2550–2562. https://doi.org/10.1175/jpo3130.1

Macdonald, A. M., & Baringer, M. O. (2013). Ocean heat transport. In International Geophysics (103, pp. 759–785). Academic Press.

Majumder, S., Schmid, C., & Halliwell, G. (2016). An observations and model-based analysis of meridional transports in the South Atlantic. *Journal of Geophysical Research: Oceans*, *121*(8), 5622–5638. https://doi.org/10.1002/2016jc011693

Masumoto, Y., Sasaki, H., Kagimoto, T., Komori, N., Ishida, A., Sasai, Y., et al. (2004). A fifty-year eddy-resolving simulation of the world ocean: Preliminary outcomes of OFES (OGCM for the Earth Simulator). *Journal of the Earth Simulator*, *1*, 35–56.

McCarthy, G. D., Brown, P. J., Flagg, C. N., Goni, G., Houpert, L., Hughes, C. W., et al. (2020). Sustainable observations of the AMOC: Methodology and technology. *Reviews of Geophysics*, *58*(1), e2019RG000654. https://doi.org/10.1029/2019RG000654

McCarthy, G. D., Smeed, D. A., Johns, W. E., Frajka-Williams, E., Moat, B. I., Rayner, D., et al. (2015). Measuring the Atlantic meridional overturning circulation at 26°N. *Progress in Oceanography*, *130*, 91–111. https://doi.org/10.1016/j.pocean.2014.10.006

McDonagh, E. L., & King, B. A. (2005). Oceanic fluxes in the South Atlantic. *Journal of Physical Oceanography*, *35*(1), 109–122. https://doi.org/10.1175/jpo-2666.1

Mears, C. A., Scott, J., Wentz, F. J., Ricciardulli, L., Leidner, S. M., Hoffman, R., & Atlas, R. (2019). A near-real-time version of the cross-calibrated multiplatform (CCMP) ocean surface wind velocity data set. *Journal of Geophysical Research: Oceans*, *124*(10), 6997–7010. https://doi.org/10.1029/2019jc015367

Meinen, C. S., Garzoli, S. L., Perez, R. C., Campos, E., Piola, A. R., Chidichimo, M. P., et al. (2017). Characteristics and causes of deep western boundary current transport variability at 34.5°S during 2009–2014. *Ocean Science*, *13*(1), 175–194. https://doi.org/10.5194/os-13-175-2017

Meinen, C. S., Piola, A. R., Perez, R. C., & Garzoli, S. L. (2012). Deep Western Boundary Current transport variability in the South Atlantic: Preliminary results from a pilot array at 34.5°S. *Ocean Science*, *8*(6), 1041–1054. https://doi.org/10.5194/os-8-1041-2012

Meinen, C. S., Speich, S., Perez, R. C., Dong, S., Piola, A. R., Garzoli, S. L., et al. (2013). Temporal variability of the meridional overturning circulation at 34.5°S: Results from two pilot boundary arrays in the South Atlantic. *Journal of Geophysical Research: Oceans*, *118*(C12), 6461–6478. https://doi.org/10.1002/2013JC009228

Meinen, C. S., Speich, S., Piola, A. R., Ansorge, I., Campos, E., Kersalé, M., et al. (2018). Meridional overturning circulation transport variability at 34.5°S during 2009–2017: Baroclinic and barotropic flows and the dueling influence of the boundaries. *Geophysical Research Letters*, *45*(9), 4180–4188. https://doi.org/10.1029/2018GL077408

Meinen, C. S., & Watts, D. R. (2000). Vertical structure and transport on a transect across the North Atlantic Current near 42°N: Time series and mean. *Journal of Geophysical Research*, *105*(C9), 21869–21891. https://doi.org/10.1029/2000jc900097

Menemenlis, D., Fukumori, I., & Lee, T. (2005). Using Green's functions to calibrate an ocean general circulation model. *Monthly Weather Review*, *133*(5), 1224–1240. https://doi.org/10.1175/MWR2912.1

Mulet, S., Rio, M. H., Etienne, H., Dibarboure, G., & Picot, N. (2019). The new CNES-CLS18 mean dynamic topography. *Conference presentation, OceanPredict'19, GODAEOceanView Symposium*. Retrieved from https://www.godae.org/~godae-data/OP19/posters/P9-Poster_MDT18.pdf

Perez, R. C., Garzoli, S. L., Meinen, C. S., & Matano, R. P. (2011). Geostrophic velocity measurement techniques for the meridional overturning circulation and meridional heat transport in the South Atlantic. *Journal of Atmospheric and Oceanic Technology*, *28*(11), 1504–1521. https://doi.org/10.1175/jtech-d-11-00058.1

Rhein, M., Rintoul, S. R., Aoki, S., Campos, E., Chambers, D., Feely, R. A., et al. (2013). Observations: Ocean. In T. F. Stocker, D. Qin, G. K. Plattner (Eds.), *Climate change 2013: The physical science basis* (pp. 255–316). Cambridge University Press.

Rousselet, L., Cessi, P., & Forget, G. (2020). Routes of the upper branch of the Atlantic meridional overturning circulation according to an ocean state estimate. *Geophysical Research Letters*, *47*(18), e2020GL089137. https://doi.org/10.1029/2020GL089137

Rühs, S., Schwarzkopf, F. U., Speich, S., & Biastoch, A. (2019). Cold vs. warm route – sources for the upper limb of the Atlantic meridional overturning circulation revisited in a high-resolution ocean model. *Ocean Science*, *15*(3), 489–512. https://doi.org/10.5194/os-15-489-2019

Sasaki, H., Nonaka, M., Masumoto, Y., Sasai, Y., Uehara, H. H, & Sakuma, H. (2008). An eddy-resolving hindcast simulation of the quasiglobal ocean from 1950 to 2003 on the Earth Simulator. In *High resolution numerical modelling of the atmosphere and ocean* (pp. 157–185). Springer. https://doi.org/10.1007/978-0-387-49791-4_10

Saunders, P. M., & King, B. A. (1995). Oceanic fluxes on the WOCE A11 section. *Journal of Physical Oceanography*, *25*(9), 1942–1958. https://doi.org/10.1175/1520-0485(1995)025<1942:ofotwa>2.0.co;2

Sloyan, B. M., & Rintoul, S. R. (2001). The Southern Ocean limb of the global deep overturning circulation. *Journal of Physical Oceanography*, *31*(1), 143–173. https://doi.org/10.1175/1520-0485(2001)031<0143:tsolot>2.0.co;2

Talley, L. D. (2003). Shallow, intermediate, and deep overturning components of the global heat budget. *Journal of Physical Oceanography*, *33*(3), 530–560. https://doi.org/10.1175/1520-0485(2003)033<0530:SIADOC>2.0.CO;2

Thomson, R. E., & Emery, W. J. (2014). *Data analysis methods in physical oceanography* (3rd ed., p. 728). Elsevier Science.

Valla, D., Piola, A. R., Meinen, C. S., & Campos, E. (2018). Strong mixing and recirculation in the northwestern Argentine Basin. *Journal of Geophysical Research: Oceans*, *123*(7), 4624–4648. https://doi.org/10.1029/2018JC013907

Valla, D., Piola, A. R., Meinen, C. S., & Campos, E. (2019). Abyssal transport variations in the southwest South Atlantic: First insights from a long-term observation array at 34.5°S. *Geophysical Research Letters*, *46*(12), 6699–6705. https://doi.org/10.1029/2019GL082740

Vallis, G. (2017). Barotropic and baroclinic instability. In *Atmospheric and oceanic fluid dynamics: Fundamentals and large-scale circulation* (pp. 335–378). Cambridge University Press. https://doi.org/10.1017/9781107588417.010

Watts, D. R., Sun, C., & Rintoul, S. (2001). A two-dimensional gravest empirical mode determined from hydrographic observations in the Subantarctic Front. *Journal of Physical Oceanography*, *31*(8), 2186–2209. https://doi.org/10.1175/1520-0485(2001)031<2186:atdgem>2.0.co;2

Willis, J. K., Roemmich, D., & Cornuelle, B. (2004). Interannual variability in upper ocean heat content, temperature, and thermosteric expansion on global scales. *Journal of Geophysical Research*, *109*(C12), C12036. https://doi.org/10.1029/2003jc002260

Wu, L., Cai, W., Zhang, L., Nakamura, H., Timmermann, A., Joyce, T., et al. (2012). Enhanced warming over the global subtropical western boundary currents. *Nature Climate Change*, *2*(3), 161–166. https://doi.org/10.1038/nclimate1353

Xue, J., Li, J., Sun, C., Zhao, S., Mao, J., Dong, D., et al. (2018a). Decadal-scale teleconnection between South Atlantic SST and southeast Australia surface air temperature in austral summer. *Climate Dynamics*, *50*(7–8), 2687–2703. https://doi.org/10.1007/s00382-017-3764-0

Xue, J., Sun, C., Li, J., & Mao, J. (2018b). South Atlantic forced multidecadal teleconnection to the midlatitude South Indian Ocean. *Geophysical Research Letters*, *45*, 8480–8489. https://doi.org/10.1029/2018GL078990